Past and future projected radiative effects from irrigation

Amen Al-Yaari[1], Chris Smith[2], Yi Yao[3], Kjetil Schanke Aas[4], L. Ruby Leung[5], Min-Hui Lo[6], Sonali McDermid[7], Larissa Nazarenko[8], Yadu Pokhrel[9], Yusuke Satoh[10], Tokuta Yokohata[11], and Wim Thiery[1]

[1]Department of Water and Climate, Vrije Universiteit Brussel, Brussels, Belgium
[2]Energy, Climate and Environment Program, International Institute for Applied Systems Analysis (IIASA), Laxenburg, Austria
[3]Institute for Atmospheric and Climate Science, Department of Environmental Systems Science, ETH Zurich, Zurich, Switzerland
[4]CICERO - Center for International Climate Research, Oslo, Norway
[5]Atmospheric, Climate, and Earth Sciences Division, Pacific Northwest National Laboratory, Richland, WA, USA
[6]Department of Atmospheric Sciences, National Taiwan University, Taipei, Taiwan
[7] Department of Environmental Studies, New York University, New York, NY, USA
[8]NASA Goddard Institute for Space Studies, New York, NY 10025, USA
[9]Department of Civil and Environmental Engineering, Michigan State University, East Lansing, MI, USA
[10]Japan Agency for Marine-Earth Science and Technology, Yokohama, Japan
[11]National Institute for Environmental Studies, Tsukuba, Japan

Correspondence to: Amen Al-Yaari (amen.al.yaari@vub.be)

Abstract. Irrigation is the most dominant freshwater use practice on Earth, yet its effect on the top-of-atmosphere (TOA) radiative budget remains uncertain because past estimates have relied on idealized experiments or single-model frameworks. Here we use on the Irrigation Model Intercomparison Project (IRRMIP) to provide the first multi-model quantification of irrigation-induced effective radiative forcing (ERF), defined here as the change in net TOA radiative flux including rapid atmospheric adjustments, over the historical period (1902-2014). Across seven Earth system models, under prescribed sea surface temperatures (SST), the global multi-model mean (MMM) irrigation-induced ERF is positive but small (~ 0.023 W m^{-2}). While the global signal is small, it masks regional heterogeneity: South Asia and West Central Asia exhibit higher positive ERF (~ 0.25 W m^{-2}), with spatial maps revealing coherent forcing hotspots of up to +5 W m^{-2} over the Indo-Gangetic Plain that are consistent across all models, while East Asia shows negative ERF (~ -0.03 W m^{-2}). The clear-sky ERF is greater than the all-sky ERF in most regions, indicating that cloud adjustments following irrigation may exert a negative contribution to the ERF. Correlations between historical irrigation ERF variability and its potential drivers suggest that reduced outgoing longwave radiation is the dominant control at the global scale and in South Asia and West Central Asia, while near-surface temperature, precipitable water, albedo, and cloud cover contribute with substantial regional and inter-model variability. We additionally examine future changes in net TOA radiation imbalance ($\Delta R_{n,TOA}$) from a fully coupled CMIP-style model (SSP1-2.6 and SSP3-7.0, 2015-2070) to assess whether the historical ERF pattern persists under future irrigation. A more global positive $\Delta R_{n,TOA}$ is found under the high irrigation demand pathway (SSP3-7.0) relative to

SSP1-2.6, consistent with projected differences in irrigation expansion between scenarios. These results demonstrate that irrigation's radiative influence, while small in the global mean, is regionally substantial and scenario-dependent, with implications for the attribution of regional climate change and for the design of land-based mitigation trajectories.

1 Introduction

Irrigation is the most dominant freshwater use practice globally, with its contribution to water withdrawals and food production estimated to range between 45-90% and 18-50%, respectively (Puy et al., 2025). Since 1901, the area equipped for irrigation (AEI) has expanded more than fivefold, reaching approximately 3 million km^2 by 2014 (Yao et al., 2025a). This massive expansion has profound impacts on the Earth system (Mahmood et al., 2014; Roy et al., 2007; Tuinenburg et al., 2011), altering global and regional water cycles (Puma and Cook, 2010; Wu et al., 2022), surface energy balances (Al-Yaari et al., 2022; Thiery et al., 2017), heat extremes (Mishra et al., 2020; Thiery et al., 2020; Yao et al., 2025a), and biogeochemical fluxes (Boucher et al., 2004). The primary biophysical effect is evaporative cooling, where irrigation water shifts the surface energy partition by increasing latent heat flux relative to sensible heat flux (Cook et al., 2015; Li et al., 2026; Mueller et al., 2017; Seneviratne et al., 2010).

At the Earth system scale, the evaporation of irrigation water introduces contrasting thermodynamic effects by adding additional moisture into the atmosphere (Li et al., 2022). As a greenhouse gas, this water vapor traps outgoing longwave radiation, potentially exerting a positive radiative effect (Koll and Cronin, 2018), while its eventual condensation releases latent heat directly into the atmosphere (Yang and Seidel, 2020). Consequently, irrigation can alter the vertical temperature profile by cooling the surface via the latent heat flux while simultaneously warming the mid-to-upper troposphere (Cook et al., 2015). Radiative forcing describes a change imposed on the Earth's radiation balance (Hansen et al., 1997) and can be used to predict long-term climate responses, offering insight into the key drivers of climate change (Sharma et al., 2026). A positive radiative forcing at the top of the atmosphere (RF) means a net energy gain that would exert a warming influence on the Earth's climate system, whereas a negative RF signifies a net energy loss, inducing a cooling effect (Bellouin et al., 2020; Forster et al., 2016). Boucher et al. (2004) estimated global mean RF from irrigation-induced water vapor of about +0.03 to +0.1 W/m^2 in idealized simulations (i.e., a prescribed-vapor simulations). However, the authors found a decrease in surface temperature dominated by evaporative cooling rather than by the excess greenhouse effect. Cook et al. (2015) found that RF is about +0.02 W/m^2 using GISS ModelE2 (compared to a non-irrigated control baseline scenario). This spread reflects both structural model uncertainty and differences in the representation of irrigation and its associated atmospheric adjustments, rather than a formal uncertainty range from a single statistical distribution.

The traditional stratospherically adjusted RF metric is not well suited to fully assess near-surface water vapor perturbations in climate models because it requires the tropospheric state (including humidity) to remain fixed (Forster et al., 2016). As a

result, tropospheric radiative adjustments, which have been shown to play an important role in the response to irrigation forcing (Sherwood et al., 2018), are not accounted for (Sherwood et al., 2015). Myhre et al. (2013) introduced the Effective RF (ERF), which includes rapid tropospheric adjustments and is a better predictor of long-term temperature change than RF (Michou et al., 2020; Ramaswamy et al., 2018). Since then, ERF has become widely used to quantify radiative forcing and adjustments across climate models (Smith et al., 2020). To our knowledge, global estimates of irrigation-induced ERF still rely on a limited number of modelling frameworks or single-model studies (e.g., Boucher et al., 2004; Gormley-Gallagher et al., 2022; Sherwood et al., 2018). Consequently, the global-scale magnitude of irrigation-driven greenhouse forcing remains highly uncertain (Li et al., 2022).

Using the Community Earth System Model (CESM 1.2.2), Sherwood et al. (2018) estimated a total global ERF of -0.10 to +0.05 W/m² from anthropogenic near-surface water-vapor emissions (mainly from irrigation). This is opposite in sign to what is expected from an increased water vapor greenhouse effect, which was explained by the negative rapid adjustments due to an increase in low cloud amount, and because the increased moisture rains out before reaching radiatively sensitive altitudes (Sherwood et al., 2018). Using the same model with an interactive irrigation module but without transient irrigation, Gormley-Gallagher et al. (2022) found that irrigation-induced ERF is about +0.05 W/m². While these studies offered new insights into irrigation-induced ERF, they were restricted to single-model perspectives and used a diversity of modelling approaches to estimate irrigation-induced ERF, challenging disentangling structural model uncertainties from uncertainties in the water vapor flow to the atmosphere.

To address these structural uncertainties and consolidate our understanding of irrigation-climate interactions, the Irrigation Model Intercomparison Project (IRRMIP) was established (Yao et al., 2025a, 2025c, 2025b). IRRMIP provides a multi-model framework involving state-of-the-art coupled climate and Earth system models (ESMs), including the Community Earth System Model version 2 (CESM2; Danabasoglu et al., 2020), CESM2 with groundwater withdrawal and flow representation (hereinafter referred to as CESM2_GW; Felfelani et al., 2021), the Centre National de Recherches Météorologiques Climate Model version 6 (hereinafter referred to as CNRM; Colin et al., 2023), the Energy Exascale Earth System Model Version 2 (hereinafter referred to as E3SM; Golaz et al., 2022) with active two-way coupled irrigation scheme (Zhou et al., 2020), the Model for Interdisciplinary Research on Climate INTEGrated LAND surface model version 1 (hereinafter referred to as MIROC; Yokohata et al., 2020), the NASA Goddard Institute for Space Studies (GISS) ModelE2.1G model (hereinafter referred to as NASA-GISS; Kelley et al., 2020), the Norwegian Earth System Model version 2 (hereinafter referred to as NorESM; Seland et al., 2020), and the Institute Pierre-Simon Laplace Climate Model version 6 (IPSL-CM6; Boucher et al., 2020) with a newly developed irrigation scheme (Arboleda-Obando et al., 2024). Although IRRMIP has already been used to assess the thermal and hydrological impacts of irrigation, its multi-model ensemble has not yet been used to quantify irrigation-induced ERF. Initial IRRMIP results led by Yao et al. (2025a) have demonstrated that while irrigation reduces dry-heat extremes, it can amplify moist-heat stress and aggravate land water depletion (Yao et al., 2025c), emphasizing the complex trade-offs of irrigation as an adaptation strategy. In this study, we leverage the IRRMIP

multi-model ensemble to provide the first quantification of irrigation-induced ERF across multiple model structures. Furthermore, we extend the analysis beyond historical simulations (1902-2014) to available future projections in one model under two Shared Socio-economic Pathways (SSPs), namely SSP1-2.6 and SSP3-7.0, which incorporate transient changes in both irrigation extent and efficiency. Because these future simulations are fully coupled (CMIP-style), in contrast to the fixed-SST (AMIP-style) historical IRRMIP experiments, note that the corresponding radiative quantity reflects both irrigation forcing and the radiative consequences of the coupled SST and circulation response and is reported here as the net TOA radiation imbalance ($\Delta R_{n,TOA}$) rather than ERF (see Section 2.2). We use this future $\Delta R_{n,TOA}$ not as a direct extension of the historical ERF time series, but as an independent test of whether the regional forcing pattern identified historically persists or intensifies under future irrigation and socioeconomic scenarios. This represents a critical gap given that future irrigation demand is projected to change under both climate warming and evolving agricultural practices. To this end, this study addresses three objectives:

I. Quantifying the historical irrigation-induced ERF (1902-2014) across seven of the eight IRRMIP models (excluding IPSL-CM6 because the atmospheric variables required to calculate ERF are unavailable) and characterizing its spatial structure and inter-model spread;

II. Identifying the dominant physical drivers of historical irrigation ERF, by analyzing the relationship between ERF and key atmospheric and surface variables: total, high, medium, and low cloud cover, surface albedo, near-surface temperature, upwelling and downwelling shortwave and longwave radiation, and precipitable water; and

III. Assessing the projected future $\Delta R_{n,TOA}$ radiation imbalance (2015-2070) under SSP1-2.6 and SSP3-7.0 to evaluate whether the regional pattern of irrigation forcing identified historically strengthens or weakens under different socioeconomic and emission trajectories.

2 Methods

2.1 The IRRMIP framework

The IRRMIP protocol consists of two transient atmosphere-land experiments with prescribed SST and sea ice (AMIP-style) over 1901-2014: with irrigation expansion and without irrigation expansion (Yao et al., 2025a). Here, we analyze simulations from seven models: CESM2, CESM2_GW, MIROC, CNRM, NorESM, NASA-GISS, and E3SM. The irrigated experiment (IRR) prescribes the transient historical evolution of irrigation extent and applies dynamically computed irrigation amounts to the land surface, whereas the experiment without irrigation expansion (NOIRR) uses identical boundary conditions but maintains irrigation conditions at their 1901 levels. The difference between the two experiments isolates the climate response to irrigation expansion, with SST and sea ice prescribed in both simulations. CESM2 is a state-of-art ESM, with the Community Land Model version 5 (CLM5) as the land model, the Community Atmosphere Model version 6 (CAM6) as the atmosphere model, and the Model for Scale Adaptive River Transport (MOSART) as the routing

mode (Yao et al., 2025a). In CESM2_GW, parameterizations for aquifer pumping and an intercell lateral groundwater interaction are implemented (Yao et al., 2025c). NorESM shares with CESM2 the same land system model (CLM5) and atmosphere model (CAM6), except for additional developments including, but not limited to, updated chemistry, aerosol, and cloud modules. Furthermore, the irrigation schemes themselves differ across models: CNRM and NASA-GISS use external irrigation forcing, whereas the other models use soil moisture-based irrigation schemes with different triggers, timing, and amounts. However, with only seven models in total, three of which share a land component and four of which are structurally distinct, the current ensemble is too small to meaningfully partition into "shared" and "independent" subsets and statistically compare their behaviors.

The reader is kindly directed to Yao et al. (2025a, 2025b) for more detailed descriptions of the models and their irrigation schemes. Multiple ensemble members are used per model where available (five for CNRM and NASA-GISS, two for NorESM and E3SM, three for MIROC, CESM2_GW and CESM2), and the per-model ensemble mean is computed before deriving the multi-model mean. Although eight models so far contributed simulations to IRRMIP, the present analysis includes seven models (CESM2, CESM2_GW, CNRM, E3SM, MIROC, NASA-GISS, and NorESM), as the atmospheric variables required for our analysis were not available for IPSL-CM6. In Yao et al. (2025b), future irrigation projections were modelled by developing dynamic irrigation efficiency and extent scenarios explicitly tied to the SSPs, thereby moving away from the static, present-day irrigation baselines used in previous studies. To project future irrigation, the authors developed a new dataset of Irrigation Techniques Share (ITS) aligned with two SSPs: SSP1-2.6 (a sustainable "green road" with low mitigation and adaptation challenges) and SSP3-7.0 (a "rocky road" with high challenges for both). These scenarios capture the real-world transition from traditional, highly consumptive flood irrigation to modern water-saving techniques like drip and sprinkler systems. Future changes in irrigation extent were taken from the Land Use Harmonization version 2 (LUH2) dataset, while the transition between irrigation methods, drip, sprinkler, and flood, was projected using a hydro-economic framework that classifies countries based on socioeconomic indicators (GDP, governance, urbanization, gender inequality) and hydroclimatic conditions (precipitation), assuming that wealthier and drier countries adopt efficient techniques faster. These transient ITS scenarios were then implemented in CESM2, which was extended to allow multiple irrigation techniques per crop type per grid cell, enabling yearly updates to the mix of irrigation methods (Yao et al., 2022). Fully coupled climate simulations were performed for 2015-2074 under both scenarios, each with three ensemble members, with and without transient irrigation.

2.2 Computation of ERF

The TOA net radiation flux is defined as FSNT - FLNT, where FSNT is the net all-sky shortwave flux at top of model and FLNT is the net all-sky longwave flux at top of model. The TOA ERF is calculated as the difference in net radiative flux between the IRR and NOIRR experiments. It is computed as follows:

$$ERF = (FSNT_{IRR} - FLNT_{IRR}) - (FSNT_{NOIRR} - FLNT_{NOIRR}) \quad (1)$$

For each model, ERF is computed per ensemble member and then averaged across members. Note that CNRM does not provide FSNT and FLNT directly but instead provides the CMIP standard-name variables rsdt (TOA incident shortwave radiation), rsut (TOA outgoing shortwave radiation), and rlut (TOA outgoing longwave radiation); for this model, FSNT was computed as rsdt - rsut and FLNT was assumed equal to rlut.

This ERF computation is valid for the historical AMIP-style simulations, where SST and sea ice are prescribed, as already mentioned. The future scenario simulations (CESM2 SSP1-2.6 and SSP3-7.0) are fully coupled, allowing SST to respond to the irrigation perturbation. We therefore report this future period quantity as the net TOA radiation imbalance ($\Delta R_{n,TOA}$) rather than ERF.

The multi-model mean (MMM) ERF is computed by averaging each model's ensemble-mean ERF over 1902-2014 at the global scale (GLO) and regionally for South Asia (SAS), western North America (WNA), central North America (CNA), the Mediterranean (MED), East Asia (EAS), and western central Asia (WCA). For the spatial maps of historical ERF (Fig. 3), the period (1981-2014) mean is shown on a common grid, regridded using linear interpolation to the CESM2 grid. For the future spatial maps (Fig. 8), the 2050-2070 mean is used, following the analysis period adopted by Yao et al. (2025b). A 21-year, first-degree Savitzky-Golay smoothing filter (Savitzky and Golay, 1964) is applied to all time series prior to display (Figs.1-2,5-6), to highlight decadal to multidecadal variability while suppressing interannual noise. Finally, only five models, CNRM, CESM2_GW, MIROC, NASA-GISS, and E3SM, provide more variables beyond FSNT and FLNT, allowing the computation of clear-sky ERF and assessment of potential physical drivers of ERF.

3 Results and Discussion

3.1 Regional and global historical annual mean ERF

At the global scale, the irrigation-induced all-sky ERF remains small throughout the entire period (Fig. 1A), with MMM reported in Table 1, being about +0.023 W m^{-2}. The direction of the global mean ERF is consistent with previous studies (e.g., Boucher et al., 2004; Cook et al., 2015; Gormley-Gallagher et al., 2022), though the magnitudes are not identical, but opposite in sign to Sherwood et al. (2018). Sherwood et al. (2018) and Gormley-Gallagher et al. (2022) reported opposite irrigation impacts on ERF. However, the perturbations considered in the two studies are not directly comparable. Sherwood et al. imposed an idealized near-surface water-vapor source without accounting for the associated surface evaporative cooling, whereas Gormley-Gallagher et al. represented irrigation interactively through the land model but ignored irrigation expansion. The IRRMIP models, in contrast, represent transient irrigation extent throughout the simulation period, thereby accounting for the strong irrigation expansion from 1901 to 2014 concentrated in hot spots like South Asia (SAS), East Asia (EAS), and Central North America (CNA). The IRRMIP models simulate a broad range of global irrigation water withdrawal (IWW; 900-4000 km^3/yr during the post-2000 period), but the temporal trend of simulations with transient

irrigation extent generally aligns with that of AEI, as illustrated in Yao et al. (2025a). This broad range of IWW simulated by the IRRMIP model may be explained by the different representations of irrigation in these models. Despite the expansion of irrigated areas since 1901 (Fig. 1H), the strengthening positive ERF over SAS and WCA is offset by a negative response over EAS, together with mixed or near-zero responses elsewhere. Thus, the global-mean ERF remains small and shows no clear long-term trend.

The global irrigation-induced ERF (+0.023 W m^{-2}) is smaller in magnitude than the total anthropogenic ERF over 1750-2019 at 2.72 [1.96 to 3.48] W m^{-2}, the ERF of greenhouse gases at 3.84 [3.46 to 4.22] W m^{-2}, and the aerosol ERF at -1.3 [-2.0 to -0.6] W m^{-2} over 1750-2014 (Forster et al., 2023).

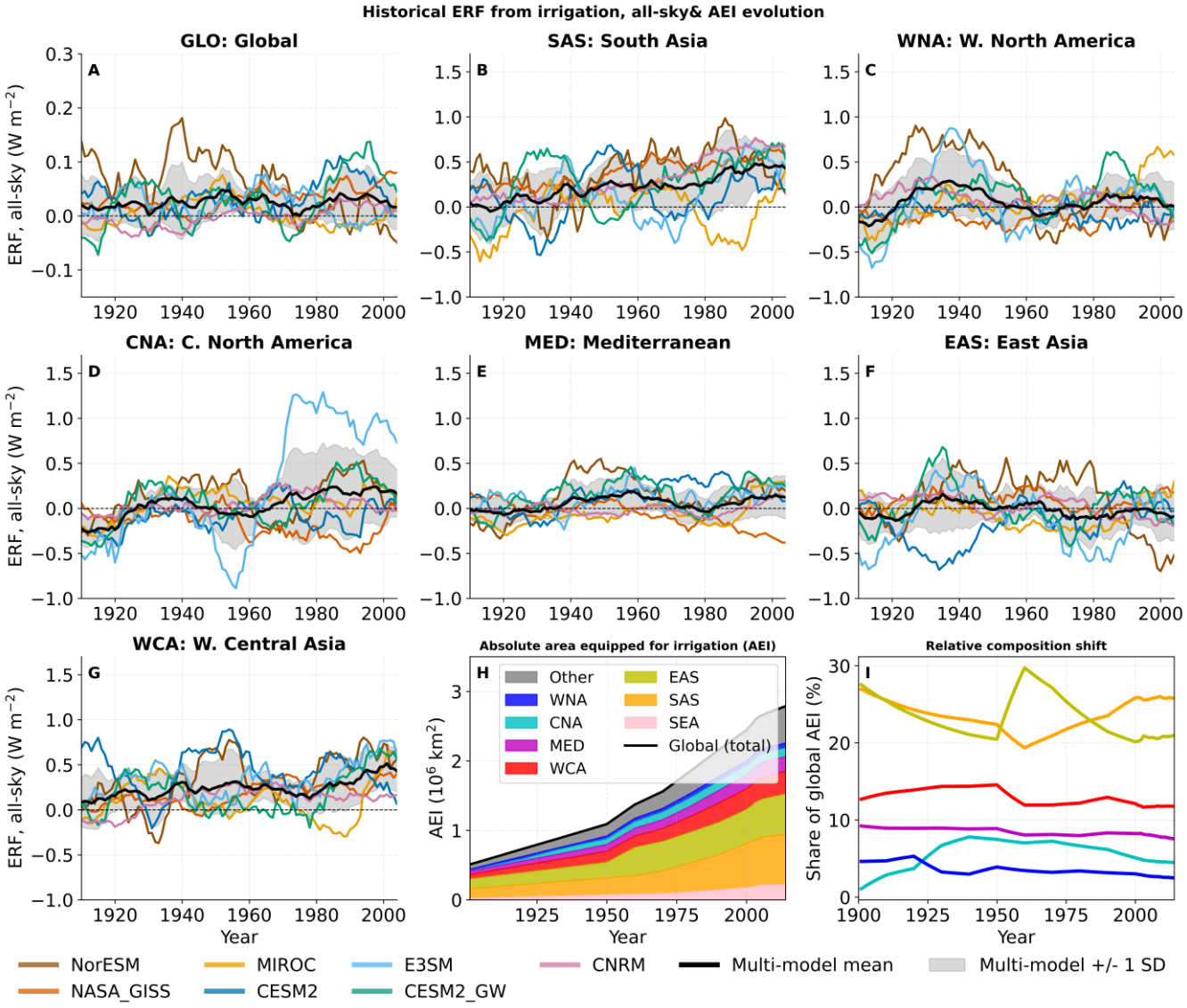


Figure 1. (A-G) Global and regional annual mean all-sky ERF (W m^{-2}) from irrigation for each model and the multi-model mean (black line) over the historical period (1902-2014). A 21-year Savitzky-Golay smoother is applied and shading indicates inter-model spread (±1 standard deviation). (H) Global and regional time series of area equipped for irrigation (AEI), adapted from Yao et al. (2025a). (I) Relative composition shift in regional contributions to global AEI, expressed as the share (%) of each region's irrigated area relative to the global total over 1901-2014, illustrating how the regional balance of irrigation expansion has changed over time. To minimize edge effects introduced by the 21-year Savitzky-Golay filter, the first and last 10 years of the record are not shown. The spatial extent of the regions is shown in Fig. 3A. GLO, SAS, WNA, CNA, MED, EAS, SEA, and WCA stand for global, South Asia, western North America, central North America, the Mediterranean, East Asia, Southeast Asia, and western central Asia, respectively (Iturbide et al., 2020).

Regionally (see Fig. 3A for the region's boundaries), the historical ERF time series under all-sky conditions in SAS shows a gradual intensification of the irrigation signal through the 20th century, broadly tracking the global expansion of irrigated area (Fig. 1B, H). Irrigation rapidly expanded during the 20th century, leading to a progressive modification of the atmospheric column above irrigated regions (Yao et al., 2025a). The rate of ERF change over SAS accelerates after approximately 1950, consistent with the rapid post-war expansion of irrigation infrastructure in Asia. South Asia (SAS; Fig. 1B) shows the strongest and most coherent positive ERF signal, rising progressively from near zero in the early 20th century to values approaching 0.5 W m^{-2} by the 1980s for NorESM, with a historical MMM of +0.22 W m^{-2}. This is consistent with the massive expansion of irrigated area in the Indian subcontinent, as evident in Fig. 1 I: SAS evolved from contributing a modest share of global irrigated area to dominating it by the early 21st century. According to Yao et al. (2025a), SAS has the highest simulated IWW across all IRRMIP models, accounting for approximately one-third of global IWW after 2000 (32.4-35.8% in CESM2, 31.4-35.1% in CESM2_GW, 27.5-41.8% in E3SM, and 32.8-35.1% in NorESM). The large positive ERF (i.e., warming influence) here may reflect reduced TOA outgoing longwave from increased atmospheric moisture, which outweighs the shortwave cooling effect of enhanced cloud cover, a pattern noted for northern India in earlier single-model studies (Cook et al., 2015). West central Asia (WCA; Fig. 1G) displays a similarly rising positive historical ERF MMM of +0.24 W m^{-2}, associated with extensive irrigation in Central Asian river basins. Despite having a smaller area equipped for irrigation than EAS, WCA has the second-highest IWW consumption, highlighting that simulated IWW depends not only on irrigated area but also on factors such as background climate conditions (Yao et al., 2025a). The Mediterranean (MED; Fig. 1E) region shows weaker ERF (+0.05 W m^{-2}) but is stable over time. Western North America (WNA; Fig. 1C), CNA (Fig. 1D) and EAS (Fig. 1F) show a smaller ERF. Overall, while the global ERF from irrigation is small, the regional ERF can reach magnitudes of 0.4 W m^{-2} in SAS and WCA, comparable to the magnitude of aerosol ERF signals in South Asia (Sharma et al., 2026). This has implications for detection and attribution: irrigation and aerosol forcing may partially co-vary in time and space in heavily industrialized and irrigated regions, making their separation in observational records challenging (van Oldenborgh et al., 2018).

Table 1: Period-mean ERF (historical, AMIP) and $\Delta R_{n,TOA}$ (future scenarios, coupled CMIP) from irrigation (IRR minus NOIRR) in W m^{-2}, derived from annual means. Historical simulations cover 1902-2014; future SSP scenarios cover 2015-2070. Multi-model mean (MMM) and 95% confidence interval are shown. The confidence intervals (CI) values are based on a t-distribution across the seven models. GLO, SAS, WNA, CNA, MED, EAS, and WCA stand for global, South Asia, western North America, central North America, the Mediterranean, East Asia, and western central Asia, respectively. Note: historical ERF and future $\Delta R_{n,TOA}$ are not directly comparable in magnitude, owing to differing experimental design (fixed-SST AMIP-style vs. fully coupled CMIP-style simulations, Section 2.2).

Model	Global	South Asia	W. North America	C. North America	Mediterranean	East Asia	W. Central Asia
Historical period mean ERF (W m^{-2}; 1902-2014)							
NASA-GISS	0.039	0.396	-0.111	-0.136	-0.081	0.068	0.185
MIROC	0.006	-0.017	0.115	0.059	-0.020	-0.011	0.165
CESM2	0.028	0.113	-0.056	-0.062	0.133	-0.150	0.425
CNRM	-0.004	0.320	0.056	0.026	-0.008	0.011	0.110
E3SM	0.018	0.134	-0.011	0.206	0.111	-0.173	0.353
NorESM	0.047	0.340	0.171	0.076	0.110	0.023	0.279
CESM2_GW	0.025	0.281	0.023	0.015	0.136	0.012	0.182
MMM Mean	**0.023**	**0.224**	**0.027**	**0.026**	**0.054**	**-0.031**	**0.243**
MMM ±95% CI	**±0.016**	**±0.138**	**±0.090**	**±0.100**	**±0.082**	**±0.085**	**±0.105**
Future scenario period mean $\Delta R_{n,TOA}$ (W m^{-2}; 2015-2070)							
CESM2-SSP3-7.0	0.022	1.593	0.336	0.255	0.293	-0.234	0.868
CESM2-SSP1-2.6	-0.014	1.322	-0.052	0.069	0.021	-0.193	0.988

Changes in atmospheric water vapor and cloud cover can affect TOA radiative responses (Colman et al., 1997). When repeating the same analysis under clear-sky conditions, a more pronounced irrigation-induced ERF emerges across all regions (Fig. 2). Globally, the clear-sky forcing exhibits a systematic upward trajectory, particularly after the mid-20th century. This amplification, also true over SAS, WCA, and CNA, when moving from all-sky to clear-sky diagnostics, indicates that cloud-related adjustments contribute negatively to the all-sky ERF. The larger clear-sky ERF suggests that irrigation-induced cloud changes partially offset the positive clear-sky radiative effects of water vapor. These cloud-related effects may involve enhanced shortwave reflection and changes in cloud amount or distribution associated with enhanced surface evaporation and latent heat flux, which can modify atmospheric stability and cloud formation. In particular, increased partitioning of available energy into latent rather than sensible heat flux may reduce atmospheric boundary layer (ABL) warming and alter its vertical development, stability or moisture conditions, potentially favoring low-cloud formation and thereby contributing to the cloud-mediated cooling response (Qian et al., 2013; Rappin et al., 2022; Tiengou et al.,

2026). In EAS, the clear-sky signal is weakly positive or near zero while the all-sky signal is negative, suggesting that cloud-associated effects may regulate or even reverse the sign of the regional ERF.

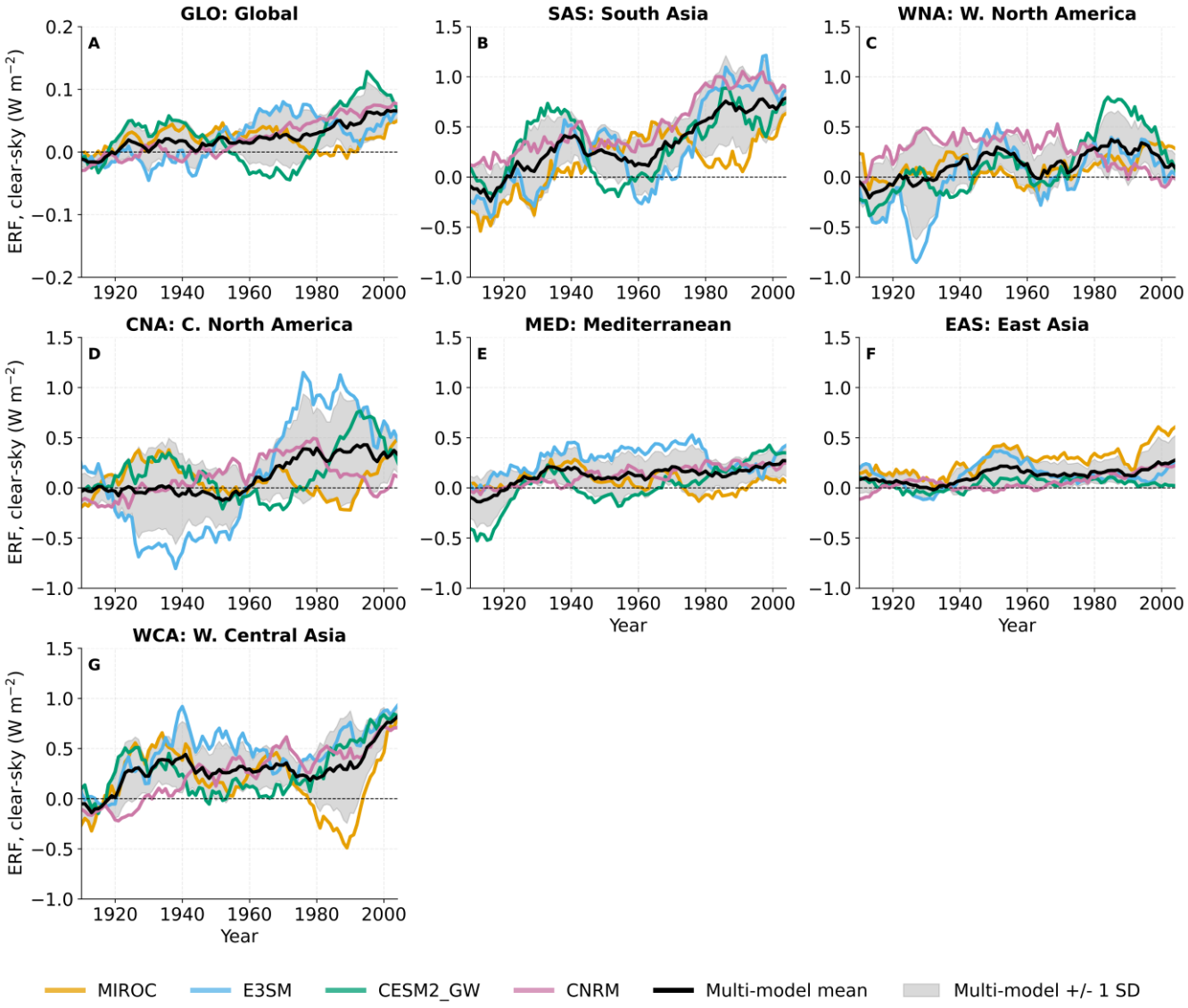


Figure 2. same as Fig. 1 but under clear-sky conditions and for only the models that provide the required clear-sky radiation variables. To minimize the edge effects introduced by the 21-year Savitzky-Golay filter, the first and last 10 years of the record are not shown.

Furthermore, we present the spatial distribution of the historical (1981-2014) annual mean irrigation-induced ERF across individual models (Fig. 3 A-G), and MMM (Fig. 3H). The spatial maps reveal that while the global mean ERF is small,

irrigation imposes strong, highly localized radiative signatures that are concentrated over major agricultural basins. The spatial structure confirms why SAS and WCA dominate the regional time-series signals. A spatially coherent positive ERF hotspot (+1 to +5 W m^{-2}) extends across northern India and Pakistan, a feature that is replicated across all models. This intense positive patch explains the increase in the SAS region seen after 1950 in Fig 2. Some of the models exhibit also patches of warming over the High Plains aquifer in the United States. Over Eastern and Central China, the models display a negative forcing signature (-1 to -3 W m-2), especially in NorESM and E3SM. This regional cooling explains the small downward trend noted in the EAS time series (Table 1). Hatched areas (Fig. 3H), where at least six of the seven models agree on sign of change and |MMM| > 1 W/m², over the Indo-Gangetic Plain confirm that the regional intensification captured throughout the 20th century time series is a coherent climate response across independent modelling frameworks. The spatial co-location of these positive and negative anomalies explains the global-scale buffering effect, showing that the near-zero global mean ERF is not an indication of weak thermodynamic activity, but rather the result of distinct regional forcing patterns counterbalancing one another.

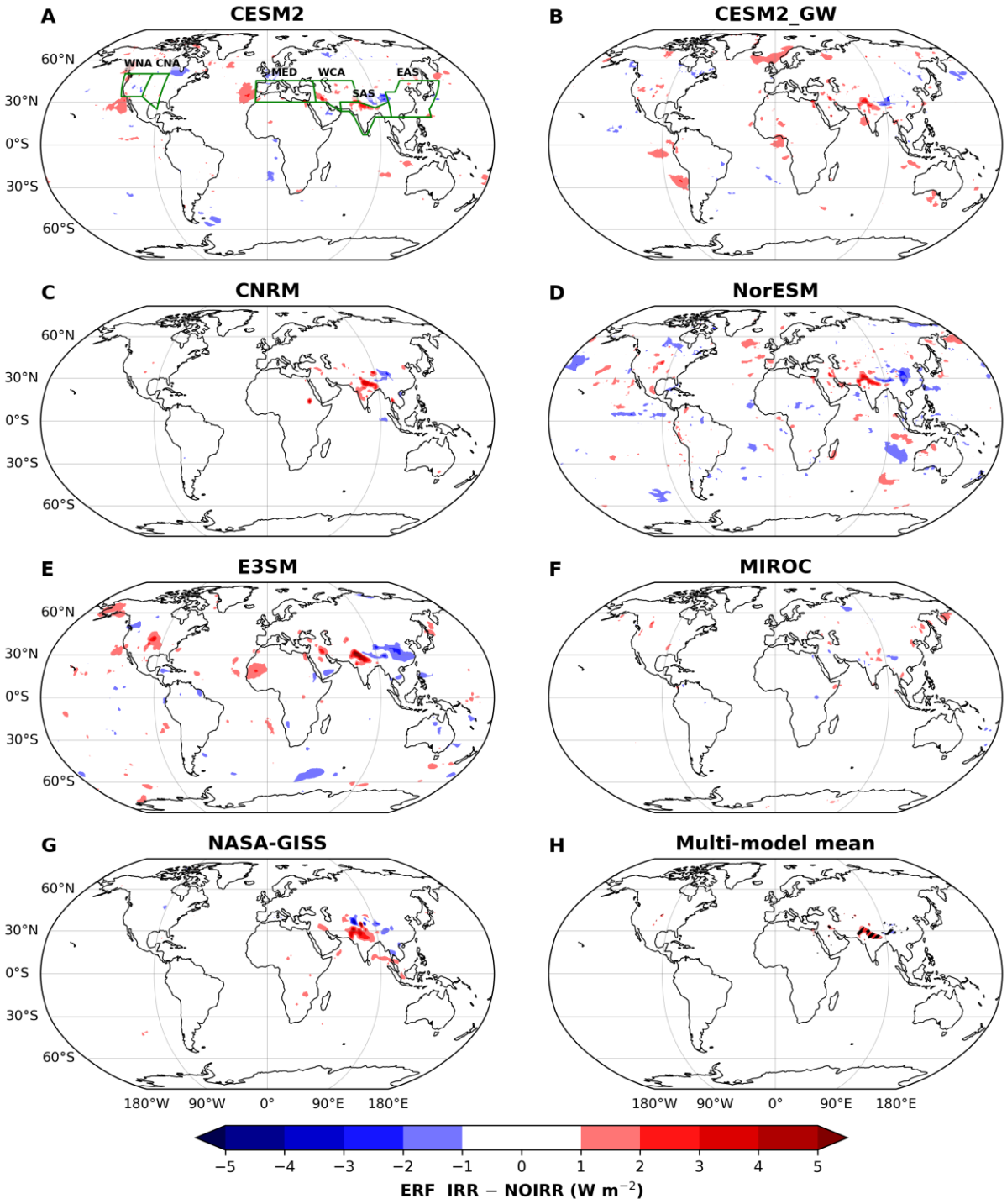


Figure 3. Global maps of the 1981-2014 mean effective radiative forcing from irrigation (ERF; W m^{-2}) for each of the seven IRRMIP models (CESM2, CESM2_GW, CNRM, NorESM, NASA-GISS, MIROC, and E3SM) and their multi-model mean. Hatches mark areas where at least six out of seven models agree on the sign.

Several models also show isolated positive (> +1 W m^{-2}) and negative (< -1 W m^{-2}) ERF patches over the oceans. Under clear-sky conditions, most of these oceanic features disappear, with ERF values generally remaining between -1 and +1 W m^{-2} (Fig. 4). This contrast indicates that the oceanic anomalies in the all-sky fields may be associated with cloud-related radiative effects. This contribution should, however, be interpreted with caution, given structural uncertainties in cloud representation across models. At the same time, the multi-model consistency of several key spatial patterns and physical relationships provides confidence that the main features of the irrigation-induced radiative response are not specific to a single model formulation. All-sky versus clear-sky comparison provides a diagnostic estimate of the net cloud contribution rather than a process attribution, and its magnitude remains model dependent.

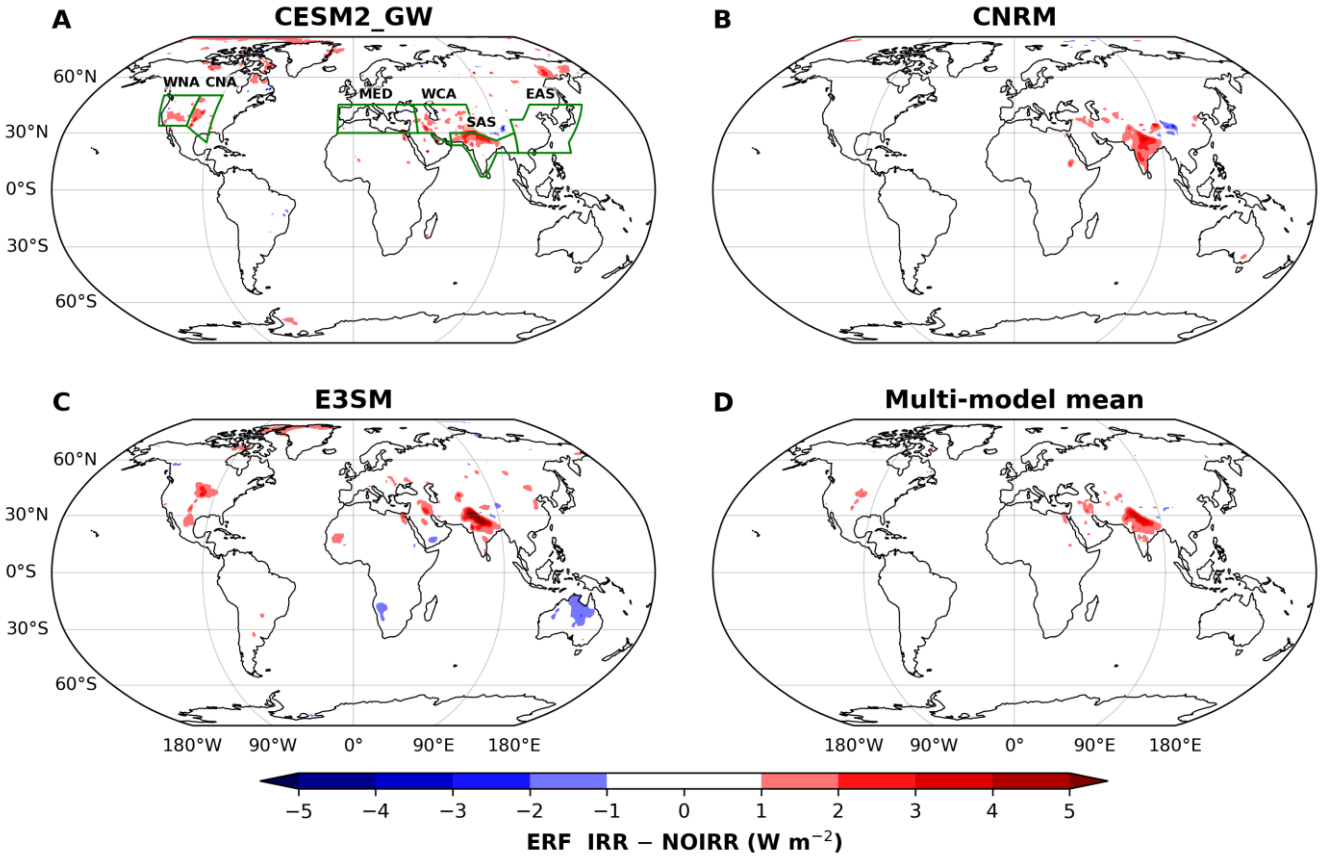


Figure 4. Same as Figure 3, but under clear-sky conditions and only for CESM2_GW, CNRM, and E3SM.

3.2 Physical drivers and feedback mechanisms

To uncover the physical processes governing the historical irrigation-induced ERF, we examine its co-variation with a suite of land and atmospheric variables, available only from CNRM, CESM2_GW, MIROC, NASA-GISS, and E3SM. Following

the definition of ERF (eq. 1), we analyze inter-model correlations across various regions (Fig. 5). For each variable, we calculate its irrigation-induced change as the difference between IRR and NOIRR simulations. Figure 5 displays the correlations over 1910-2004 between irrigation-induced ERF and the corresponding irrigation-induced changes in total cloud cover, high cloud cover, medium cloud cover, low cloud cover, near-surface temperature, precipitable water, TOA net SW radiation, TOA Outgoing Longwave Radiation (LW), surface downwelling SW, surface upwelling SW, and surface albedo. In the following, we focus on variables for which all five models exhibit a robust agreement in the sign of correlation.

The models' ERF is negatively correlated ($< \sim -0.5$, $p < 0.001$) with the irrigation-induced change in TOA LW at the global scale (Fig. 5A), as well as in SAS (Fig. 5B) and WCA (Fig. 5G). Physically, this is an expected relationship: since ERF is defined as the irrigation-induced change in FSNT - FLNT, a reduction in outgoing LW (which decreases FLNT) increases ERF if FSNT remains constant. As established in literature, irrigation cools the surface via enhanced latent heat flux and simultaneously increases atmospheric moisture (Boucher et al., 2004; Mahmood et al., 2014; Thiery et al., 2017).

Both processes may reduce outgoing LW, as increased water vapor enhances the local greenhouse effect, while a cooler surface emits less thermal radiation (Li et al., 2022). Interestingly, this correlation reverses in WNA (Fig. 5C) and CNA (Fig. 5D), suggesting that in these regions, other components of the TOA energy balance (likely SW changes) dominate the ERF response. The relationship between ERF and outgoing longwave radiation is not uniform across all regions. For instance, MED and EAS do not show the same clear relationship as SAS and WCA. In EAS and MED, the models show contrasting relationships between ERF and outgoing LW, with some exhibiting negative correlations and others positive relationships. This inter-model spread likely reflects differences in the relative contributions of longwave water-vapor effects and shortwave radiative effects associated with cloud and surface changes, as well as differences in the representation of cloud processes and parameterizations across models.

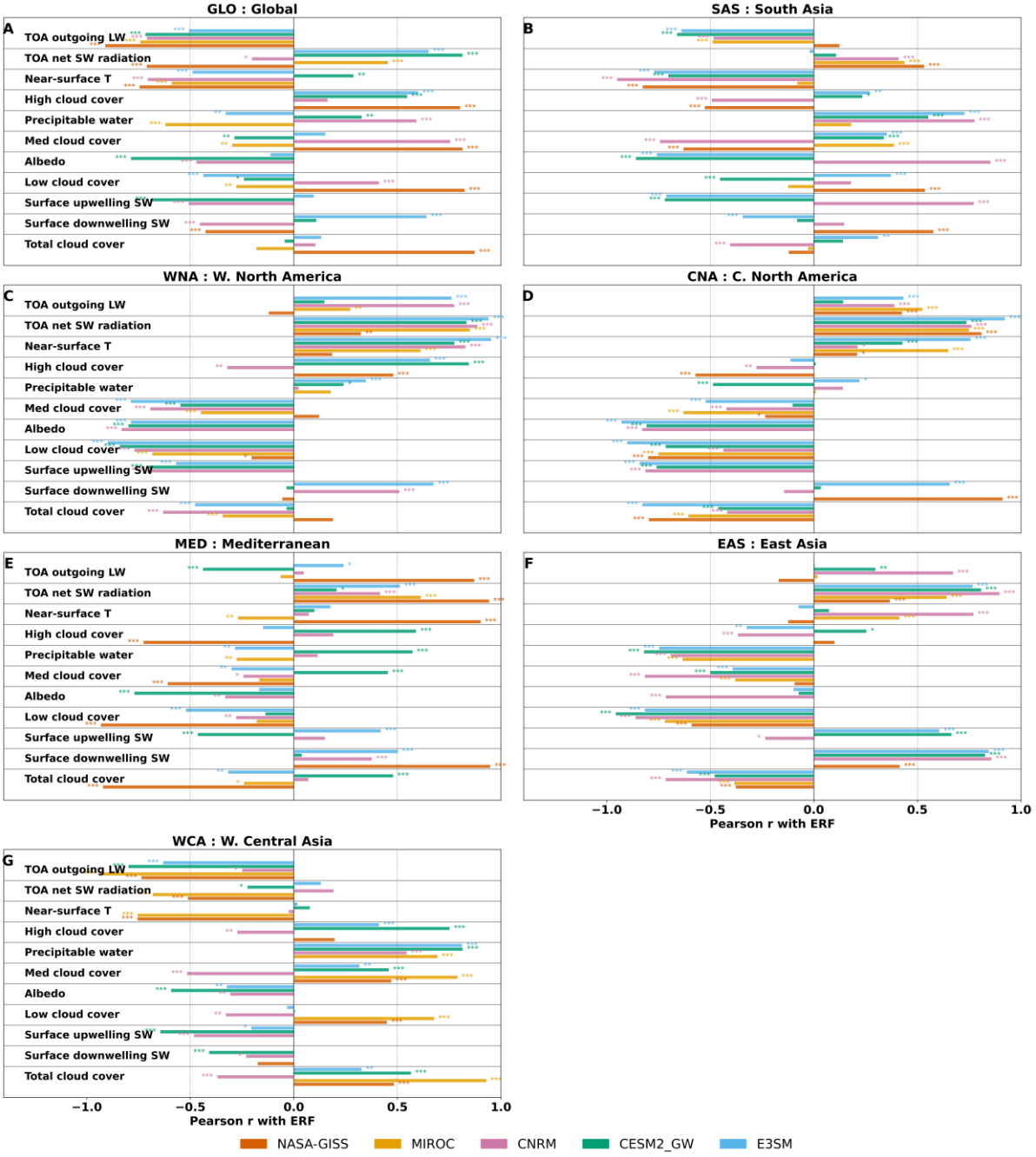


Figure 5. Pearson correlations between 21-year smoothed irrigation-induced Effective Radiative Forcing (ERF) and TOA outgoing longwave (LW) flux, TOA net shortwave (SW) flux, near-surface air temperature (T), high cloud cover, precipitable water, medium (med) cloud cover, albedo, low cloud cover, surface upwelling SW flux, surface downwelling SW flux, and total cloud cover under all-sky conditions during 1910-2004. Correlation significance levels are denoted by asterisks ($p < 0.05$, ** $p < 0.01$, *** $p < 0.001$).

Similarly to LW, near-surface temperature (T) correlates negatively with ERF in SAS (all models agree on sign). This relationship is consistent with irrigation-induced cooling being associated with a stronger positive ERF response, particularly through the reduction in outgoing LW radiation. Water vapor acting as a greenhouse gas that traps upwelling LW radiation and radiates it back to the Earth's surface as downward longwave radiation. Although this process tends to increase surface energy input, the increased energy availability appears to be partitioned to latent heat flux through enhanced evapotranspiration, resulting in a net decrease in surface temperature. The high inter-model agreement in SAS (Fig. 5B) compared to the disagreement at the global scale (Fig. 5A) indicates that the SAS signal is a robust regional feature that is likely obscured by divergent responses in other regions when averaged globally (Cook et al., 2011). In contrast, models agree on a positive correlation over WNA and CNA, reflecting a regime where higher temperatures coincide with stronger ERF, possibly due to dominant SW feedbacks or different evaporative regimes in these semi-arid climates (Singh et al., 2018).

Precipitable water exhibits a positive correlation with ERF across SAS ($r > 0.5$), WCA, and WNA. The positive correlation indicates that models with larger irrigation-induced increases in precipitable water also tend to exhibit larger positive irrigation-induced ERF. Again, this effect is consistent with physical understanding, where irrigation-induced water vapor increases regional greenhouse trapping, thereby modulating the TOA energy balance (Boucher et al., 2004). Regarding surface albedo, the models show negative correlations globally and across most regions, indicating that decreases in albedo linked to surface wetting are generally associated with higher ERF through enhanced absorption of solar radiation. However, reductions in albedo can also trigger atmospheric adjustments (Laguë et al., 2021; Tang et al., 2025). For example, Laguë et al. (2021) showed that lower land surface albedo increases cloud cover, accompanied by enhanced precipitation, leading to greater reflection of TOA incoming shortwave radiation and enhanced longwave trapping over land. These opposing radiative effects may partially offset one another, thereby moderating the net ERF.

Similarly, cloud ERF interactions show regional variability: high cloud cover correlate positively with ERF at the global scale, consistent with enhanced longwave trapping (Deutloff et al., 2025). Conversely, there is no agreement among the models considering the relationship between low cloud cover and ERF. Low cloud cover changes correlate negatively with ERF in WNA, CNA, MED, and EAS, consistent with a cooling contribution from increased low cloud cover through enhanced reflection of incoming shortwave radiation (Ceppi et al., 2026; Hill et al., 2018), with agreement in sign across all models. In SAS (Fig. 5B), correlation signs between changes in high, medium, and low cloud cover and ERF diverge across models. This is consistent with findings over India showing that the radiative effects of irrigation-induced changes in cloud cover can vary with cloud type, season, and location (Chou et al., 2018). Overall, the irrigation-induced ERF is a complex metric because irrigation-induced surface cooling often decouples from TOA energy balance shifts (Boucher et al., 2004; Gormley-Gallagher et al., 2022; Mahmood et al., 2014). This regional heterogeneity aligns with previous findings that local climate responses are determined by the interplay between local energy balance and regional circulation patterns (Cook et al., 2011; de Vrese et al., 2016; Singh et al., 2018).

3.3 Regional and global future annual mean radiation imbalance

As mentioned earlier, unlike the historical period, the future scenario simulations are fully coupled (CMIP-style) runs in which SST responds to the irrigation perturbation; the IRR-NOIRR difference in net TOA radiation therefore reflects both irrigation's forcing and the radiative consequences of the coupled climate response (Section 2.2). We report this quantity as the net TOA radiation imbalance ($\Delta R_{n,TOA}$) and use it here not as a direct extension of the historical ERF time series, but as an independent test of whether the regional pattern identified for historical ERF persists or intensifies under future irrigation and socioeconomic scenarios. Because of the differing experimental design, the magnitudes of $\Delta R_{n,TOA}$ and historical ERF (Table 1) should not be compared directly; comparisons across the two periods should be limited to spatial and regional patterns, not absolute values.

Figure 6 shows that $\Delta R_{n,TOA}$, under all-sky conditions, in the future (post-2014), the CESM2-SSP3-7.0 (red) and CESM2-SSP1-2.6 (blue) scenarios diverge only modestly from the historical ERF, suggesting that changes in irrigation extent alone may not strongly shift the global energy budget under either pathway, although there is a very small negative trend under SSP126. The future $\Delta R_{n,TOA}$ signal from CESM2 (Fig. 6) shows similar regional spatial patterns to the historical ERF, with SAS and WCA exhibiting the largest magnitudes, exceeding 1 W m^{-2} for most of the 2016-2070 period, while the remaining regions remain below 1 W m^{-2} throughout.

In the future period, SSP3-7.0 (higher warming, less efficient irrigation) tends to produce a more positive $\Delta R_{n,TOA}$ compared to SSP1-2.6 over most of the regions, especially over MED, consistent with greater irrigation water demand under a warmer and drier trajectory (Yao et al., 2025b). Yao et al. (2025b) have projected that annual irrigation water withdrawal decreases under SSP1-2.6 but increases under SSP3-7.0, with new irrigation hotspots emerging in Africa. The fact that the SSP3-7.0 scenario sustains a stronger positive $\Delta R_{n,TOA}$ in heavily irrigated regions aligns with that trajectory: more water applied means stronger latent heat and moisture feedback, maintaining or amplifying the regional radiation imbalance signal into the second half of the 21st century. Under SSP3-7.0, the $\Delta R_{n,TOA}$ signal is projected to be stronger in magnitude than under SSP1-2.6 by 2050-2070 over all regions (Table 1), consistent with higher projected irrigation demand under higher warming and continued agricultural intensification. Under SSP1-2.6, a partial stabilization or weakening of the $\Delta R_{n,TOA}$ is projected in some models, reflecting reduced irrigation extent under stringent climate mitigation pathways where improved efficiency reduces water application rates. The negative trends over EAS are likely to persist until 2070.

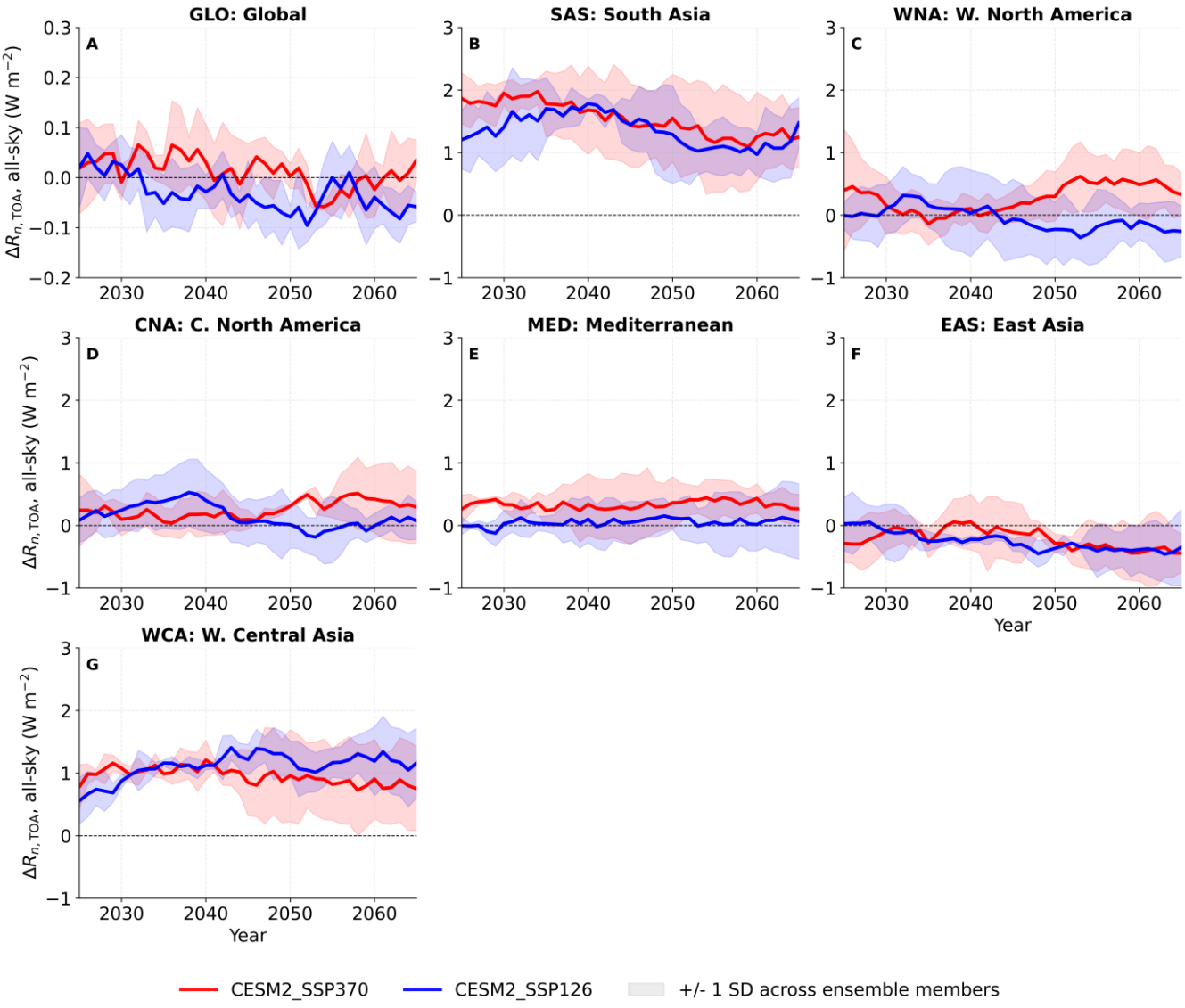


Figure 6. (A-G) Global and regional annual mean radiation imbalance ($\Delta R_{n,TOA}$, W m^{-2}) under all-sky conditions from irrigation under future scenarios SSP1-2.6 and SSP3-7.0 (2015-2070). A 21-year Savitzky-Golay smoother is applied. Shading indicates spread across ensemble members (±1 standard deviation).

Compared to the global values of $\Delta R_{n,TOA}$ under all-sky conditions, with SSP3-7.0 staying mostly slightly positive and SSP1-2.6 dipping more often below zero (Fig. 6A), clear-sky global values (Fig. 7A) are systematically higher than all-sky for both scenarios. This indicates that cloud adjustments pull the global signal down, consistent with what was found for the historical ERF, thus clouds are exerting a net negative (cooling) contribution to $\Delta R_{n,TOA}$ in the future runs too.

SAS (Fig. 7B) is the dominant regional signal under all-sky conditions (~1-2.5 W/m² vs <1 W/m² elsewhere), with higher clear-sky values (~1.5-2.5 W/m²) than all-sky for the same years, and the decline over time is similar in shape. In both sky conditions, SSP3-7.0 (red, higher-irrigation-demand) leads SSP1-2.6 (blue) early on, but they cross around 2040-2050, and SSP1-2.6 ends up higher by 2065-2070. Under clear-sky conditions, $\Delta R_{n,TOA}$ in WCA (Fig. 7G) rises steadily from ~0.9 W m^{-2} in 2016 to ~ 1.5 W m^{-2} by the 2040s, again with SSP3-7.0 leading initially before the scenarios converge and reverse ordering after approximately 2045. Figs. 6E and 7E show that $\Delta R_{n,TOA}$ over MED has a smaller magnitude, with SSP3-7.0 systematically exceeding SSP1-2.6 throughout most of the simulation period under both sky conditions but remains stable throughout the period. East Asia exhibits a distinct radiative regime in which the competing longwave and shortwave effects of irrigation are more closely balanced. Irrigation-induced moistening tends to increase atmospheric longwave trapping, producing a positive clear-sky contribution, but this effect is relatively weak compared with the strong positive response over SAS and WCA. At the same time, the historical analysis shows a consistent negative relationship between low- and medium-level cloud changes and ERF over EAS, indicating that cloud-related shortwave reflection can offset part of the longwave effect. Under the future CESM2 simulations, the clear-sky $\Delta Rn_{,TOA}$ in EAS changes from weakly positive to weakly negative around 2030-2040 in both scenarios, suggesting that the balance between the competing radiative components evolves as the background climate and irrigation-induced hydrological response change. In addition, the small difference between the all-sky and clear-sky responses over EAS suggests that the net cloud contribution is insufficient to substantially modify the already weak clear-sky signal, indicating that non-cloud processes also contribute to the negative radiative response. Overall, across all regions, clear-sky $\Delta R_{n,TOA}$ is consistently equal to or larger than all-sky $\Delta R_{n,TOA}$, indicating that cloud adjustments exert a systematic damping influence on the $\Delta R_{n,TOA}$ response to irrigation in the future projections, mirroring the all-sky/clear-sky relationship found for the historical ERF.

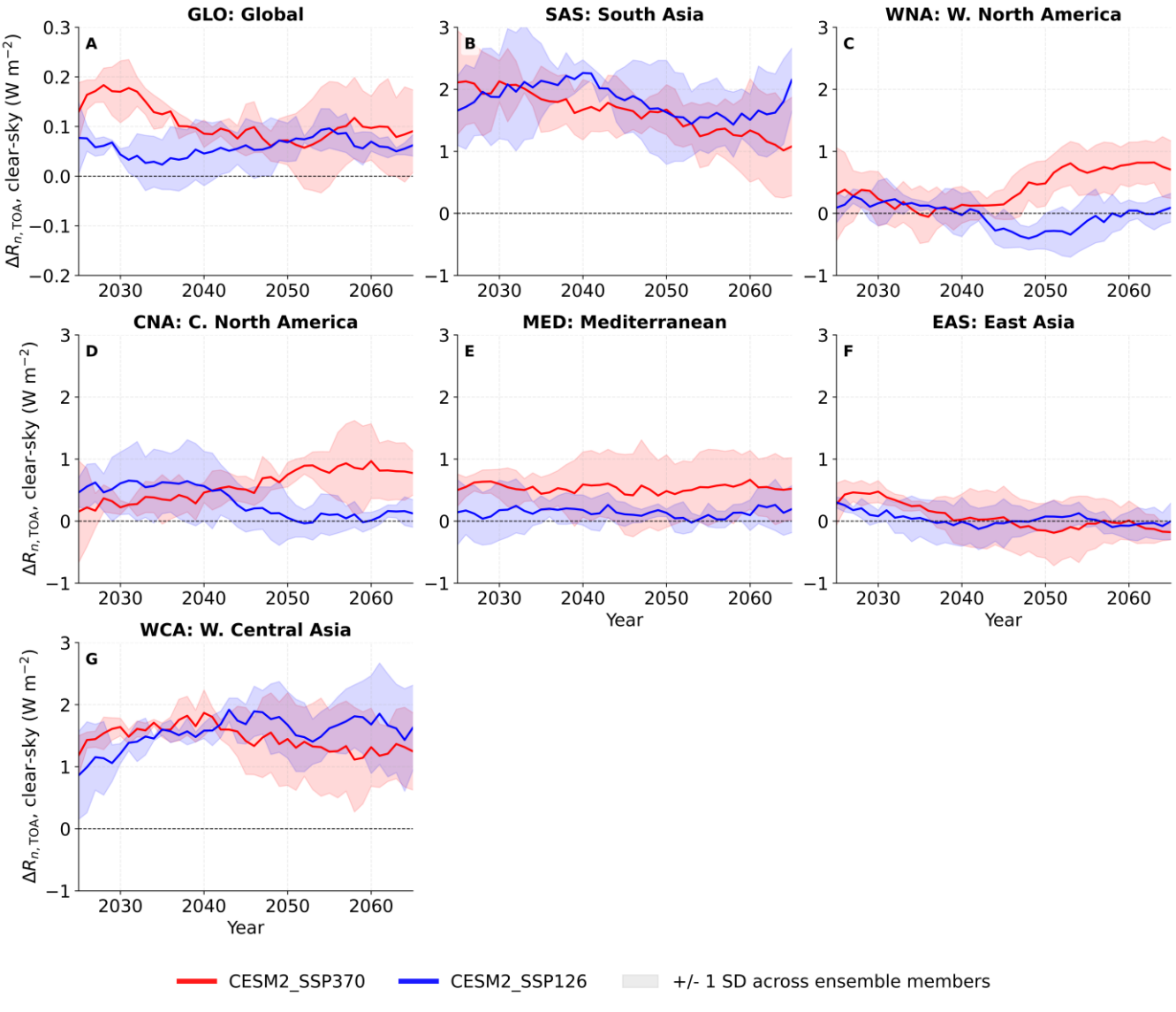


Figure 7. same as Fig. 6 but under clear-sky conditions.

Figure 8 shows the spatial distribution of the irrigation-induced radiation imbalance (IRR - NOIRR) under two future SSPs from CESM2, under all-sky (Fig. 8A, B) and clear-sky (Fig. 8C, D) conditions, averaged over 2050-2070. The spatial structure of the projected future $\Delta R_{n,TOA}$ broadly resembles the historical pattern. Under SSP1-2.6 and SSP3-7.0, the positive $\Delta R_{n,TOA}$ over SAS intensifies relative to the historical mean, while Central Asia and parts of Sub-Saharan Africa show emerging irrigation signals associated with the projected expansion of irrigated areas in those regions. Future land-use scenarios should more explicitly represent the evolution of irrigation practices and that climate models should account for

irrigation as a climate-relevant land-management forcing. Under all-sky conditions (Fig. 8A, B), the spatial pattern is heterogeneous with both positive and negative anomalies of comparable magnitude scattered across irrigated and non-irrigated regions (particularly over the oceans). SSP3-7.0 shows somewhat stronger positive signals over SAS and WCA compared to SSP1-2.6, which instead exhibits a large negative anomaly (-3 to -5 W m^{-2}) over the tropical Atlantic and Indian Ocean, an ocean region where no irrigation occurs. This ocean signal may indicate cloud radiative adjustments driven remotely by irrigation-induced moisture and circulation changes rather than a direct local forcing (Laguë et al., 2022; Wey et al., 2015). Under the clear-sky (Fig. 8C, D), over the major irrigated regions including the Indo-Gangetic Plain and WCA, a consistent positive $\Delta R_{n,TOA}$ of +1 to +3 W m^{-2} emerges clearly in both scenarios. The strong ocean anomalies in Fig. 8A, B under all-sky conditions are almost absent under clear-sky conditions (Fig. 8C, D), confirming they are cloud-mediated responses rather than direct water vapor forcing (Laguë et al., 2021). The clear-sky signal is also more spatially coherent between SSP3-7.0 and SSP1-2.6, with SSP3-7.0 producing somewhat larger positive values over SAS and Central Asia, consistent with greater irrigation water application under the higher-emission scenario.

Cook et al. (2015) showed that the relative magnitude of the longwave and shortwave processes causes regional increases in energy availability at the TOA over northern India. It seems that this is also true under future conditions: SAS and WCA are consistently positive in clear-sky ERF, while EAS shows weaker and more mixed signals, consistent with a notable role of cloud-shortwave compensation there. Overall, the total all-sky $\Delta R_{n,TOA}$ from irrigation is not simply the water vapor greenhouse effect. The cloud adjustments can be of comparable or greater magnitude and opposite sign, making the all-sky $\Delta R_{n,TOA}$ highly model- and scenario-dependent. This is consistent with findings from Sherwood et al. (2018), who showed that increases in water vapor greenhouse effect from near-surface emissions (as in irrigation) are partially offset by increases in reflectance from low-level clouds, leading to an effective radiative forcing likely near zero globally but with significant regional structure.

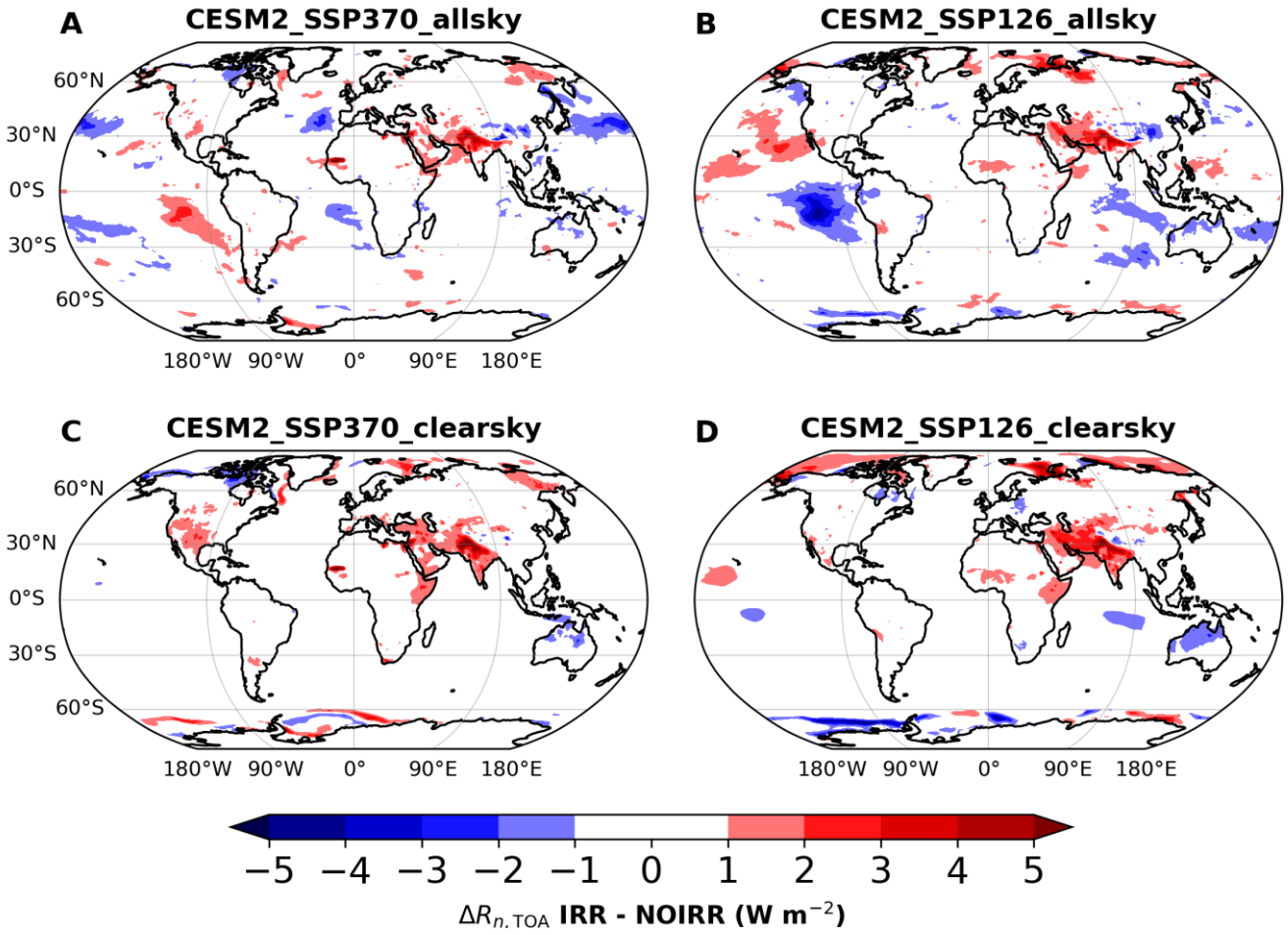


Figure 8. As Figure 3, but for the projected 2050-2070 mean of $\Delta R_{n,TOA}$ under SSP1-2.6 (right) and SSP3-7.0 (left) from CESM2 under all-sky (A and B) and clear-sky (C and D) conditions.

4. Conclusions

This study provides the first multi-model assessment of irrigation-induced ERF using the IRRMIP ensemble, spanning historical (1902-2014) simulations across seven ESMs. Three main conclusions can be drawn. First, the global mean irrigation-induced ERF (all-sky) is positive and small (MMM ≈ 0.023 W m^{-2}) with no clear historical trend, consistent with earlier single-model estimates (Boucher et al., 2004; Cook et al., 2015; Gormley-Gallagher et al., 2022) but with the opposite sign to Sherwood et al. (2018). This small global signal arises from a near-cancellation between longwave trapping by irrigation-enhanced atmospheric moisture and shortwave reflection associated primarily with cloud changes and from the offsetting contributions from regions with positive and negative ERF. This should therefore not be interpreted as evidence of

weak regional radiative responses. The small global-mean ERF may also be influenced by a low signal-to-noise ratio (Forster et al., 2016). Second, this global cancellation masks a strong regional structure. South Asia and WCA show model-consistent positive ERF reaching 1-5 W m^{-2} locally, concentrated over the Indo-Gangetic Plain, while EAS shows a persistent negative signal, confirming that irrigation can have substantial local effects. Clear-sky diagnostics indicate that cloud adjustments provide negative feedback that dampens the all-sky forcing in most regions. The analysis of potential radiative drivers further shows that ERF variability is most strongly associated with variability in outgoing longwave radiation on global scale. The fact that some relationships (e.g., the sign of the temperature-ERF correlation) differ between SAS and the semi-arid regions of North America and MED highlights that no single physical mechanism generalizes across all irrigated regions. Third, the future projections indicate that the $\Delta R_{n,TOA}$ radiation imbalance associated with irrigation is sensitive to the socioeconomic pathway governing irrigation extent and efficiency: SSP3-7.0, which projects higher irrigation water demand, produces a stronger positive $\Delta R_{n,TOA}$ than SSP1-2.6 across the globe by 2070. This suggests that the radiative consequences of irrigation are not fixed but will likely evolve with both climate trajectory and water-management choices and should therefore be considered explicitly in the land-use components of future climate scenarios.

Several areas for improvement remain and should be explored in future studies. (i) The analysis of potential radiative drivers in Section 3.2 is based on only five of the seven IRRMIP models (CNRM, CESM2_GW, NASA-GISS, MIROC, and E3SM). (ii) The none-identical ERF values of the models may reflect differences in irrigation, cloud, and convection parameterizations. This flags parameterization diversity as a future work and recommends that future, larger multi-model irrigation ensembles be designed with explicit attention to sampling independent land-atmosphere-irrigation structures. (iii) The correlation-based driver attribution does not establish causal direction; several of the candidate drivers (e.g., cloud cover, albedo, water vapor) are themselves rapid adjustments to the same underlying perturbation rather than independent forcings, so the reported relationships should be interpreted as diagnostic of co-variation, not as a decomposition into independent causal pathways. (iv) The future scenario simulations (CESM2 under SSP1-2.6 and SSP3-7.0) are fully coupled (CMIP-style) runs, in contrast to the fixed-SST AMIP configuration used for the historical experiments. As a result, the IRR-NOIRR difference in net TOA radiation for the future period ($\Delta R_{n,TOA}$, Table 1 and Figs. 6-8) reflects both the irrigation forcing and the radiative consequences of the coupled SST/circulation response and should not be interpreted as ERF in the same sense as the historical values. We retain these coupled-run diagnostics because they offer a preliminary indication of how the net radiative consequences of irrigation may evolve under contrasting socioeconomic pathways. However, isolating a true future ERF would require fixed-SST (AMIP-style) future experiments or a dedicated forcing-feedback decomposition, which are beyond the scope of the present study and are identified here as a priority for future work. In addition, the future projections are currently available only from CESM2, as no other IRRMIP modelling groups have performed the corresponding future irrigation experiments. Consequently, the magnitude and regional patterns of the projected responses may be influenced by CESM2 specific characteristics and should be interpreted as preliminary rather than as a robust multi-model projection. Finally, future work should prioritize expanding the diagnostic output of additional IRRMIP models to enable a more complete multi-model driver attribution, incorporating multiple models into the future-scenario analysis to test

the robustness of the SSP-dependent ERF strengthening reported here, and developing harmonized historical-future experimental protocols to remove the discontinuities currently introduced by differing irrigation parameterizations and atmosphere-only versus coupled configurations.

Code and data availability

No proprietary software was used. The IRRMIP simulations are in the process of being published publicly on the Earth System Grid Federation (ESGF) platform: https://esgf.github.io/nodes.html.

Supplement link

The link to the supplement will be included by Copernicus, if applicable.

Author contributions

A.A., C.S. and W.T. designed the study. A.A. led the writing of the paper and the preparation of the figures. C.S. performed the initial analysis of the ERF from IRRMIP models. Y.Y and W.T coordinated IRRMIP. K.S.A, M.L, S.M., L.N., L.L., Y.P., Y.S., and T.Y. performed the IRRMIP ESM simulations. All co-authors contributed to writing sections and reviewing drafts of the paper.

Competing interests

The contact author has declared that none of the authors has any competing interests.

Disclaimer

Copernicus Publications remains neutral with regard to jurisdictional /claims made in the text, published maps, institutional affiliations, or any other geographical representation in this paper. While Copernicus Publications makes every effort to include appropriate place names, the final responsibility lies with the authors. Views expressed in the text are those of the authors and do not necessarily reflect the views of the publisher.

Acknowledgements

This work was supported by the European Commission Marie Curie Postdoctoral Fellowship grant #101106066 (A.A.). W.T. received funding from the European Research Council (ERC) under the European Union's Horizon Framework research and innovation programme (grant agreement No 101076909; 'LACRIMA' project). W.T. and C.S. were supported by the European Union's Horizon Europe programme (grant agreement No 101295156; 'FUTURA'). T.Y. was supported by the Program for the Advanced Studies of Climate Change Projection (SENTAN, grant number JPMXD0722681344). Y.S. was supported by JSPS KAKENHI (Grant Number 22K14101). The computational resources and services used in this work for the storage and analysis of IRRMIP data were provided by the VSC (Flemish Supercomputer Center), funded by the Research Foundation-Flanders (FWO) and the Flemish Government-department EWI. M.H.L. was supported by the Academia Sinica Scholar Award (AS-ASSA-114-01), with computational resources provided by the National Center for High-performance Computing (NCHC), NARLabs, Taiwan. K.S.A. was supported by Research Council of Norway (grant no. 352405).

Financial support

This work was supported by the European Commission Marie Curie Postdoctoral Fellowship grant #101106066 (A.A.). W.T. received funding from the European Research Council (ERC) under the European Union's Horizon Framework research and innovation programme (grant agreement No 101076909; 'LACRIMA' project). W.T. and C.S. were supported by the European Union's Horizon Europe programme (grant agreement No 101295156; 'FUTURA'). T.Y. was supported by the Program for the Advanced Studies of Climate Change Projection (SENTAN, grant number JPMXD0722681344). Y.S. was supported by JSPS KAKENHI (Grant Number 22K14101). The computational resources and services used in this work for the storage and analysis of IRRMIP data were provided by the VSC (Flemish Supercomputer Center), funded by the Research Foundation-Flanders (FWO) and the Flemish Government-department EWI. M.H.L. was supported by the Academia Sinica Scholar Award (AS-ASSA-114-01), with computational resources provided by the National Center for High-performance Computing (NCHC), NARLabs, Taiwan. K.S.A. was supported by Research Council of Norway (grant no. 352405).

Review statement

The review statement will be added by Copernicus Publications listing the handling editor as well as all contributing referees according to their status anonymous or identified.

References

Al-Yaari, A., Ducharne, A., Thiery, W., Cheruy, F., Lawrence, D., 2022. The Role of Irrigation Expansion on Historical Climate Change: Insights From CMIP6. https://doi.org/10.1029/2022EF002859

Arboleda-Obando, P.F., Ducharne, A., Yin, Z., Ciais, P., 2024. Validation of a new global irrigation scheme in the land surface model ORCHIDEE v2.2. Geosci. Model Dev. 17, 2141–2164. https://doi.org/10.5194/gmd-17-2141-2024

Bellouin, N., Davies, W., Shine, K.P., Quaas, J., Mülmenstädt, J., Forster, P.M., Smith, C., Lee, L., Regayre, L., Brasseur, G., Sudarchikova, N., Bouarar, I., Boucher, O., Myhre, G., 2020. Radiative forcing of climate change from the Copernicus reanalysis of atmospheric composition. Earth Syst. Sci. Data 12, 1649–1677. https://doi.org/10.5194/essd-12-1649-2020

Boucher, O., Myhre, G., Myhre, A., 2004. Direct human influence of irrigation on atmospheric water vapour and climate. Clim. Dyn. 22, 597–603. https://doi.org/10.1007/s00382-004-0402-4

Boucher, O., Servonnat, J., Albright, A.L., Aumont, O., Balkanski, Y., Bastrikov, V., Bekki, S., Bonnet, R., Bony, S., Bopp, L., Braconnot, P., Brockmann, P., Cadule, P., Caubel, A., Cheruy, F., Codron, F., Cozic, A., Cugnet, D., D'Andrea, F., Davini, P., de Lavergne, C., Denvil, S., Deshayes, J., Devilliers, M., Ducharne, A., Dufresne, J.-L., Dupont, E., Éthé, C., Fairhead, L., Falletti, L., Flavoni, S., Foujols, M.-A., Gardoll, S., Gastineau, G., Ghattas, J., Grandpeix, J.-Y., Guenet, B., Guez, E., Lionel, Guilyardi, E., Guimberteau, M., Hauglustaine, D., Hourdin, F., Idelkadi, A., Joussaume, S., Kageyama, M., Khodri, M., Krinner, G., Lebas, N., Levavasseur, G., Lévy, C., Li, L., Lott, F., Lurton, T., Luyssaert, S., Madec, G., Madeleine, J.-B., Maignan, F., Marchand, M., Marti, O., Mellul, L., Meurdesoif, Y., Mignot, J., Musat, I., Ottlé, C., Peylin, P., Planton, Y., Polcher, J., Rio, C., Rochetin, N., Rousset, C., Sepulchre, P., Sima, A., Swingedouw, D., Thiéblemont, R., Traore, A.K., Vancoppenolle, M., Vial, J., Vialard, J., Viovy, N., Vuichard, N., 2020. Presentation and Evaluation of the IPSL-CM6A-LR Climate Model. J. Adv. Model. Earth Syst. 12, e2019MS002010. https://doi.org/10.1029/2019MS002010

Ceppi, P., Wilson Kemsley, S., Andersen, H., Andrews, T., Kramer, R.J., Nowack, P., Wall, C.J., Zelinka, M.D., 2026. Emerging low-cloud feedback and adjustment in global satellite observations. Atmos. Chem. Phys. 26, 4153–4171. https://doi.org/10.5194/acp-26-4153-2026

Chou, C., Ryu, D., Lo, M.-H., Wey, H.-W., Malano, H.M., 2018. Irrigation-Induced Land–Atmosphere Feedbacks and Their Impacts on Indian Summer Monsoon. J. Clim. 31, 8785–8801. https://doi.org/10.1175/JCLI-D-17-0762.1

Colin, J., Decharme, B., Cattiaux, J., Saint-Martin, D., 2023. Groundwater Feedbacks on Climate Change in the CNRM Global Climate Model. J. Clim. 36, 7599–7617. https://doi.org/10.1175/JCLI-D-22-0767.1

Colman, R.A., Power, S.B., McAvaney, B.J., 1997. Non-linear climate feedback analysis in an atmospheric general circulation model. Clim. Dyn. 13, 717–731. https://doi.org/10.1007/s003820050193

Cook, B.I., Puma, M.J., Krakauer, N.Y., 2011. Irrigation induced surface cooling in the context of modern and increased greenhouse gas forcing. Clim. Dyn. 37, 1587–1600. https://doi.org/10.1007/s00382-010-0932-x

Cook, B.I., Shukla, S.P., Puma, M.J., Nazarenko, L.S., 2015. Irrigation as an historical climate forcing. Clim. Dyn. 44, 1715–1730. https://doi.org/10.1007/s00382-014-2204-7

Danabasoglu, G., Lamarque, J.-F., Bacmeister, J., Bailey, D.A., DuVivier, A.K., Edwards, J., Emmons, L.K., Fasullo, J., Garcia, R., Gettelman, A., Hannay, C., Holland, M.M., Large, W.G., Lauritzen, P.H., Lawrence, D.M., Lenaerts, J.T.M., Lindsay, K., Lipscomb, W.H., Mills, M.J., Neale, R., Oleson, K.W., Otto-Bliesner, B., Phillips, A.S., Sacks, W., Tilmes, S., van Kampenhout, L., Vertenstein, M., Bertini, A., Dennis, J., Deser, C., Fischer, C., Fox-Kemper, B., Kay, J.E., Kinnison, D., Kushner, P.J., Larson, V.E., Long, M.C., Mickelson, S., Moore, J.K., Nienhouse, E., Polvani, L., Rasch, P.J., Strand, W.G., 2020. The Community Earth System Model Version 2 (CESM2). J. Adv. Model. Earth Syst. 12, e2019MS001916. https://doi.org/10.1029/2019MS001916

de Vrese, P., Hagemann, S., Claussen, M., 2016. Asian irrigation, African rain: Remote impacts of irrigation. Geophys. Res. Lett. 43, 3737–3745. https://doi.org/10.1002/2016GL068146

Deutloff, J., Buehler, S.A., Brath, M., Naumann, A.K., 2025. Insights on Tropical High-Cloud Radiative Effect From a New Conceptual Model. J. Adv. Model. Earth Syst. 17, e2024MS004615. https://doi.org/10.1029/2024MS004615

Felfelani, F., Lawrence, D.M., Pokhrel, Y., 2021. Representing Intercell Lateral Groundwater Flow and Aquifer Pumping in the Community Land Model. Water Resour. Res. 57, e2020WR027531. https://doi.org/10.1029/2020WR027531

Forster, P.M., K, A., T, S., W, C., Dufresne, J.-L., D, F., D.j, L., T, M., M.d, P., M, Watanabe, M, Wild, H, Z.A., 2023. The Earth's Energy Budget, Climate Feedbacks and Climate Sensitivity. Cambridge University Press, p. 923. https://doi.org/10.1017/9781009157896.009

Forster, P.M., Richardson, T., Maycock, A.C., Smith, C.J., Samset, B.H., Myhre, G., Andrews, T., Pincus, R., Schulz, M., 2016. Recommendations for diagnosing effective radiative forcing from climate models for CMIP6. J. Geophys. Res. Atmos. 121, 12,460-12,475. https://doi.org/10.1002/2016JD025320

Golaz, J.-C., Van Roekel, L.P., Zheng, X., Roberts, A.F., Wolfe, J.D., Lin, W., Bradley, A.M., Tang, Q., Maltrud, M.E., Forsyth, R.M., Zhang, C., Zhou, T., Zhang, K., Zender, C.S., Wu, M., Wang, H., Turner, A.K., Singh, B., Richter, J.H., Qin, Y., Petersen, M.R., Mametjanov, A., Ma, P.-L., Larson, V.E., Krishna, J., Keen, N.D., Jeffery, N., Hunke, E.C., Hannah, W.M., Guba, O., Griffin, B.M., Feng, Y., Engwirda, D., Di Vittorio, A.V., Dang, C., Conlon, L.M., Chen, C.-C.-J., Brunke, M.A., Bisht, G., Benedict, J.J., Asay-Davis, X.S., Zhang, Y., Zhang, M., Zeng, X., Xie, S., Wolfram, P.J., Vo, T., Veneziani, M., Tesfa, T.K., Sreepathi, S., Salinger, A.G., Reeves Eyre, J.E.J., Prather, M.J., Mahajan, S., Li, Q., Jones, P.W., Jacob, R.L., Huebler, G.W., Huang, X., Hillman, B.R., Harrop, B.E., Foucar, J.G., Fang, Y., Comeau, D.S., Caldwell, P.M., Bartoletti, T., Balaguru, K., Taylor, M.A., McCoy, R.B., Leung, L.R., Bader, D.C., 2022. The DOE E3SM Model Version 2: Overview of the Physical Model and Initial Model Evaluation. J. Adv. Model. Earth Syst. 14, e2022MS003156. https://doi.org/10.1029/2022MS003156

Gormley-Gallagher, A.M., Sterl, S., Hirsch, A.L., Seneviratne, S.I., Davin, E.L., Thiery, W., 2022. Agricultural management effects on mean and extreme temperature trends. Earth Syst. Dyn. 13, 419–438. https://doi.org/10.5194/esd-13-419-2022

Hansen, J., Sato, M., Ruedy, R., 1997. Radiative forcing and climate response. J. Geophys. Res. Atmos. 102, 6831–6864. https://doi.org/10.1029/96JD03436

Hill, P.G., Allan, R.P., Chiu, J.C., Bodas-Salcedo, A., Knippertz, P., 2018. Quantifying the Contribution of Different Cloud Types to the Radiation Budget in Southern West Africa. J. Clim. 31, 5273–5291. https://doi.org/10.1175/JCLI-D-17-0586.1

Intergovernmental Panel on Climate Change (IPCC) (Ed.), 2023. The Earth's Energy Budget, Climate Feedbacks and Climate Sensitivity, in: Climate Change 2021 – The Physical Science Basis: Working Group I Contribution to the Sixth Assessment Report of the Intergovernmental Panel on Climate Change. Cambridge University Press, Cambridge, pp. 923–1054. https://doi.org/10.1017/9781009157896.009

Iturbide, M., Gutiérrez, J.M., Alves, L.M., Bedia, J., Cerezo-Mota, R., Cimadevilla, E., Cofiño, A.S., Di Luca, A., Faria, S.H., Gorodetskaya, I.V., Hauser, M., Herrera, S., Hennessy, K., Hewitt, H.T., Jones, R.G., Krakovska, S., Manzanas, R., Martínez-Castro, D., Narisma, G.T., Nurhati, I.S., Pinto, I., Seneviratne, S.I., van den Hurk, B., Vera, C.S., 2020. An update of IPCC climate reference regions for subcontinental analysis of climate model data: definition and aggregated datasets. Earth Syst. Sci. Data 12, 2959–2970. https://doi.org/10.5194/essd-12-2959-2020

Kelley, M., Schmidt, G.A., Nazarenko, L.S., Bauer, S.E., Ruedy, R., Russell, G.L., Ackerman, A.S., Aleinov, I., Bauer, M., Bleck, R., Canuto, V., Cesana, G., Cheng, Y., Clune, T.L., Cook, B.I., Cruz, C.A., Del Genio, A.D., Elsaesser, G.S., Faluvegi, G., Kiang, N.Y., Kim, D., Lacis, A.A., Leboissetier, A., LeGrande, A.N., Lo, K.K., Marshall, J., Matthews, E.E., McDermid, S., Mezuman, K., Miller, R.L., Murray, L.T., Oinas, V., Orbe, C., García-Pando, C.P., Perlwitz, J.P., Puma, M.J., Rind, D., Romanou, A., Shindell, D.T., Sun, S., Tausnev, N., Tsigaridis, K., Tselioudis, G., Weng, E., Wu, J., Yao, M.-S., 2020. GISS-E2.1: Configurations and Climatology. J. Adv. Model. Earth Syst. 12, e2019MS002025. https://doi.org/10.1029/2019MS002025

Koll, D.D.B., Cronin, T.W., 2018. Earth's outgoing longwave radiation linear due to H2O greenhouse effect. Proc. Natl. Acad. Sci. 115, 10293–10298. https://doi.org/10.1073/pnas.1809868115

Laguë, M.M., Quetin, G.R., Boos, W.R., 2022. Downwind control of oceanic air by land: the land wake and its sensitivity to CO2. Environ. Res. Lett. 17, 104045. https://doi.org/10.1088/1748-9326/ac9702

Laguë, M.M., Swann, A.L.S., Boos, W.R., 2021. Radiative Feedbacks on Land Surface Change and Associated Tropical Precipitation Shifts. J. Clim. 34, 6651–6672. https://doi.org/10.1175/JCLI-D-20-0883.1

Li, H., Lo, M.-H., Peel, M.C., Ryu, D., Thiery, W., Zhang, Y., 2026. Local and Remote Impacts of Regional Irrigation on Near-Surface Temperature. J. Geophys. Res. Atmos. 131, e2026JD046366. https://doi.org/10.1029/2026JD046366

Li, H., Lo, M.-H., Ryu, D., Peel, M., Zhang, Y., 2022. Possible Increase of Air Temperature by Irrigation. Geophys. Res. Lett. 49, e2022GL100427. https://doi.org/10.1029/2022GL100427

Mahmood, R., Pielke Sr., R.A., Hubbard, K.G., Niyogi, D., Dirmeyer, P.A., McAlpine, C., Carleton, A.M., Hale, R., Gameda, S., Beltrán-Przekurat, A., Baker, B., McNider, R., Legates, D.R., Shepherd, M., Du, J., Blanken, P.D., Frauenfeld, O.W., Nair, U. s., Fall, S., 2014. Land cover changes and their biogeophysical effects on climate. Int. J. Climatol. 34, 929–953. https://doi.org/10.1002/joc.3736

Michou, M., Nabat, P., Saint-Martin, D., Bock, J., Decharme, B., Mallet, M., Roehrig, R., Séférian, R., Sénési, S., Voldoire, A., 2020. Present-Day and Historical Aerosol and Ozone Characteristics in CNRM CMIP6 Simulations. J. Adv. Model. Earth Syst. 12, e2019MS001816. https://doi.org/10.1029/2019MS001816

Mishra, V., Ambika, A.K., Asoka, A., Aadhar, S., Buzan, J., Kumar, R., Huber, M., 2020. Moist heat stress extremes in India enhanced by irrigation. Nat. Geosci. 13, 722–728. https://doi.org/10.1038/s41561-020-00650-8

Mueller, N.D., Rhines, A., Butler, E.E., Ray, D.K., Siebert, S., Holbrook, N.M., Huybers, P., 2017. Global Relationships between Cropland Intensification and Summer Temperature Extremes over the Last 50 Years. J. Clim. 30, 7505–7528. https://doi.org/10.1175/JCLI-D-17-0096.1

Myhre, G.D., Shindell, D., Bréon, F.M., et al, 2013. Anthropogenic and Natural Radiative Forcing Supplementary Material. In: Climate Change 2013: The Physical Science Basis. Contribution of Working Group I to the Fifth Assessment Report of the Intergovernmental Panel on Climate Change. 2013.

Puma, M.J., Cook, B.I., 2010. Effects of irrigation on global climate during the 20th century. J. Geophys. Res. Atmos. 115. https://doi.org/10.1029/2010JD014122

Puy, A., Linga, S.N., Wei, N., Flinders, S., Callow, B., Allen, G., Cross, B., Aguiló-Rivera, C., Lankford, B., 2025. Widely cited global irrigation statistics lack empirical support. PNAS Nexus 4, pgaf323. https://doi.org/10.1093/pnasnexus/pgaf323

Qian, Y., Huang, M., Yang, B., Berg, L.K., 2013. A Modeling Study of Irrigation Effects on Surface Fluxes and Land–Air–Cloud Interactions in the Southern Great Plains. J. Hydrometeorol. 14, 700–721. https://doi.org/10.1175/JHM-D-12-0134.1

Ramaswamy, V., Collins, W., Haywood, J., Lean, J., Mahowald, N., Myhre, G., Naik, V., Shine, K.P., Soden, B., Stenchikov, G., Storelvmo, T., 2018. Radiative Forcing of Climate: The Historical Evolution of the Radiative Forcing Concept, the Forcing Agents and their Quantification, and Applications. Meteorol. Monogr. 59, 14.1-14.101. https://doi.org/10.1175/AMSMONOGRAPHS-D-19-0001.1

Rappin, E.D., Mahmood, R., Nair, U.S., Sr, R.A.P., 2022. Land–Atmosphere Interactions during GRAINEX: Planetary Boundary Layer Evolution in the Presence of Irrigation. J. Hydrometeorol. 23, 1401–1417. https://doi.org/10.1175/JHM-D-21-0160.1

Roy, S.S., Mahmood, R., Niyogi, D., Lei, M., Foster, S.A., Hubbard, K.G., Douglas, E., Pielke Sr., R., 2007. Impacts of the agricultural Green Revolution–induced land use changes on air temperatures in India. J. Geophys. Res. Atmos. 112. https://doi.org/10.1029/2007JD008834

Savitzky, Abraham., Golay, M.J.E., 1964. Smoothing and Differentiation of Data by Simplified Least Squares Procedures. Anal. Chem. 36, 1627–1639. https://doi.org/10.1021/ac60214a047

Seland, Ø., Bentsen, M., Olivié, D., Toniazzo, T., Gjermundsen, A., Graff, L.S., Debernard, J.B., Gupta, A.K., He, Y.-C., Kirkevåg, A., Schwinger, J., Tjiputra, J., Aas, K.S., Bethke, I., Fan, Y., Griesfeller, J., Grini, A., Guo, C., Ilicak, M., Karset, I.H.H., Landgren, O., Liakka, J., Moseid, K.O., Nummelin, A., Spensberger, C., Tang, H., Zhang, Z., Heinze, C., Iversen, T., Schulz, M., 2020. Overview of the Norwegian Earth System Model (NorESM2) and key climate response of CMIP6 DECK, historical, and scenario simulations. Geosci. Model Dev. 13, 6165–6200. https://doi.org/10.5194/gmd-13-6165-2020

Seneviratne, S.I., Corti, T., Davin, E.L., Hirschi, M., Jaeger, E.B., Lehner, I., Orlowsky, B., Teuling, A.J., 2010. Investigating soil moisture–climate interactions in a changing climate: A review. Earth-Sci. Rev. 99, 125–161. https://doi.org/10.1016/j.earscirev.2010.02.004

Sharma, A.K., Ganguly, D., Bhattacharya, A., Sarkar, T., Sharma, A., Ghosh, S., Anand, S., Venkataraman, C., Dey, S., 2026. Assessing Aerosol Radiative Forcing and Atmospheric Absorption Over South Asia: A Multi-Model Intercomparison Study. J. Geophys. Res. Atmos. 131, e2025JD044925. https://doi.org/10.1029/2025JD044925

Sherwood, S.C., Bony, S., Boucher, O., Bretherton, C., Forster, P.M., Gregory, J.M., Stevens, B., 2015. Adjustments in the Forcing-Feedback Framework for Understanding Climate Change. Bull. Am. Meteorol. Soc. 96, 217–228. https://doi.org/10.1175/BAMS-D-13-00167.1

Sherwood, S.C., Dixit, V., Salomez, C., 2018. The global warming potential of near-surface emitted water vapour. Environ. Res. Lett. 13, 104006. https://doi.org/10.1088/1748-9326/aae018

Singh, D., McDermid, S.P., Cook, B.I., Puma, M.J., Nazarenko, L., Kelley, M., 2018. Distinct Influences of Land Cover and Land Management on Seasonal Climate. J. Geophys. Res. Atmos. 123, 12,017-12,039. https://doi.org/10.1029/2018JD028874

Smith, C.J., Kramer, R.J., Myhre, G., Alterskjær, K., Collins, W., Sima, A., Boucher, O., Dufresne, J.-L., Nabat, P., Michou, M., Yukimoto, S., Cole, J., Paynter, D., Shiogama, H., O'Connor, F.M., Robertson, E., Wiltshire, A., Andrews, T., Hannay, C., Miller, R., Nazarenko, L., Kirkevåg, A., Olivié, D., Fiedler, S., Lewinschal, A., Mackallah, C., Dix, M., Pincus, R., Forster, P.M., 2020. Effective radiative forcing and adjustments in CMIP6 models. Atmos. Chem. Phys. 20, 9591–9618. https://doi.org/10.5194/acp-20-9591-2020

Tang, S., Piao, S., Cai, W., Wang, T., Li, L.Z.X., Wang, K., Kan, F., Gui, Y., Yao, T., Li, X., 2025. Tropical Pacific Zonal Temperature Gradient Intensified by the Tibetan Plateau Surface Darkening. Geophys. Res. Lett. 52, e2025GL117253. https://doi.org/10.1029/2025GL117253

Thiery, W., Davin, E.L., Lawrence, D.M., Hirsch, A.L., Hauser, M., Seneviratne, S.I., 2017. Present-day irrigation mitigates heat extremes. J. Geophys. Res. Atmos. 122, 1403–1422. https://doi.org/10.1002/2016JD025740

Thiery, W., Visser, A.J., Fischer, E.M., Hauser, M., Hirsch, A.L., Lawrence, D.M., Lejeune, Q., Davin, E.L., Seneviratne, S.I., 2020. Warming of hot extremes alleviated by expanding irrigation. Nat. Commun. 11, 290. https://doi.org/10.1038/s41467-019-14075-4

Tiengou, P., Ducharne, A., Cheruy, F., 2026. Regional impacts of irrigation on the atmospheric and terrestrial water cycle of the Iberian Peninsula in a climate model. Earth Syst. Dyn. 17, 843–876. https://doi.org/10.5194/esd-17-843-2026

Tuinenburg, O.A., Hutjes, R.W.A., Jacobs, C.M.J., Kabat, P., 2011. Diagnosis of Local Land–Atmosphere Feedbacks in India. J. Clim. 24, 251–266. https://doi.org/10.1175/2010JCLI3779.1

van Oldenborgh, G.J., Philip, S., Kew, S., van Weele, M., Uhe, P., Otto, F., Singh, R., Pai, I., Cullen, H., AchutaRao, K., 2018. Extreme heat in India and anthropogenic climate change. Nat. Hazards Earth Syst. Sci. 18, 365–381. https://doi.org/10.5194/nhess-18-365-2018

Wey, H.-W., Lo, M.-H., Lee, S.-Y., Yu, J.-Y., Hsu, H.-H., 2015. Potential impacts of wintertime soil moisture anomalies from agricultural irrigation at low latitudes on regional and global climates. Geophys. Res. Lett. 42, 8605–8614. https://doi.org/10.1002/2015GL065883

Wu, L., Feng, J., Qin, F., Qiu, Y., 2022. Regional Climate Effects of Irrigation Over Central Asia Using Weather Research and Forecasting Model. J. Geophys. Res. Atmos. 127, e2021JD036210. https://doi.org/10.1029/2021JD036210

Yang, D., Seidel, S.D., 2020. The Incredible Lightness of Water Vapor. J. Clim. 33, 2841–2851. https://doi.org/10.1175/JCLI-D-19-0260.1

Yao, Y., Ducharne, A., Cook, B.I., De Hertog, S.J., Aas, K.S., Arboleda-Obando, P.F., Buzan, J., Colin, J., Costantini, M., Decharme, B., Lawrence, D.M., Lawrence, P., Leung, L.R., Lo, M.-H., Devaraju, N., Wieder, W.R., Wu, R.-J., Zhou, T., Jägermeyr, J., McDermid, S., Pokhrel, Y., Elling, M., Hanasaki, N., Muñoz, P., Nazarenko, L.S., Otta, K., Satoh, Y., Yokohata, T., Jin, L., Wang, X., Mishra, V., Ghosh, S., Thiery, W., 2025a. Impacts of irrigation expansion on moist-heat stress based on IRRMIP results. Nat. Commun. 16, 1045. https://doi.org/10.1038/s41467-025-56356-1

Yao, Y., Satoh, Y., van Maanen, N., Taranu, S., Keune, J., De Hertog, S.J., Lampe, S., Lawrence, D.M., Sacks, W.J., Wada, Y., Ducharne, A., Cook, B.I., Seneviratne, S.I., Liu, L., Buzan, J.R., Jägermeyr, J., Thiery, W., 2025b. Compounding future escalation of emissions- and irrigation-induced increases in humid-heat stress. Nat. Commun. 16, 9326. https://doi.org/10.1038/s41467-025-64375-1

Yao, Y., Thiery, W., Ducharne, A., Cook, B.I., Ding, A., De Hertog, S.J., Sieber, P., Aas, K.S., Arboleda-Obando, P.F., Colin, J., Costantini, M., Decharme, B., Lawrence, D.M., Lawrence, P., Leung, L.R., Lo, M.-H., Devaraju, N., Wu, R.-J., Zhou, T., Jägermeyr, J., McDermid, S.S., Pokhrel, Y., Satoh, Y., Yokohata, T., Gudmundsson, L., Seneviratne, S.I., 2025c. Irrigation-induced land water depletion aggravated by climate change. Nat. Water 3, 1424–1435. https://doi.org/10.1038/s44221-025-00529-1

Yao, Y., Vanderkelen, I., Lombardozzi, D., Swenson, S., Lawrence, D., Jägermeyr, J., Grant, L., Thiery, W., 2022. Implementation and Evaluation of Irrigation Techniques in the Community Land Model. https://doi.org/10.1029/2022MS003074

Yokohata, T., Kinoshita, T., Sakurai, G., Pokhrel, Y., Ito, A., Okada, M., Satoh, Y., Kato, E., Nitta, T., Fujimori, S., Felfelani, F., Masaki, Y., Iizumi, T., Nishimori, M., Hanasaki, N., Takahashi, K., Yamagata, Y., Emori, S., 2020. MIROC-INTEG-LAND version 1: a global biogeochemical land surface model with human water management, crop growth, and land-use change. Geosci. Model Dev. 13, 4713–4747. https://doi.org/10.5194/gmd-13-4713-2020

Zhou, T., Leung, L.R., Leng, G., Voisin, N., Li, H.-Y., Craig, A.P., Tesfa, T., Mao, Y., 2020. Global Irrigation Characteristics and Effects Simulated by Fully Coupled Land Surface, River, and Water Management Models in E3SM. J. Adv. Model. Earth Syst. 12, e2020MS002069. https://doi.org/10.1029/2020MS002069